





Unconfined gravity current interactions with orthogonal topography: Implications for combined-flow processes and the depositional record

ED KEAVNEY* , JEFF PEAKALL* , RU WANG*, DAVID M. HODGSON* ,
IAN A. KANE† , GARETH M. KEEVIL*, HELENA C. BROWN*, MICHAEL A. CLARE‡
and MIA J. HUGHES*

*School of Earth and Environment, University of Leeds, Leeds LS2 9JT, UK (E-mail: d.hodgson@leeds.ac.uk)

†Department of Earth and Environmental Science, University of Manchester, Manchester M13 9PL, UK

‡Ocean BioGeoscience, National Oceanography Centre, Southampton SO14 3ZH, UK

Associate Editor – Kyle Straub

ABSTRACT

Turbidity current behaviour is affected by interactions with seafloor topography. Changes in flow dynamics will depend on the orientation and gradient of the topography, and the magnitude and rheology of the incoming flow. A better understanding of how unconfined turbidity currents interact with topography will improve interpretations of the stratigraphic record, and is addressed herein using three-dimensional flume tank experiments with unconfined saline density currents that enter a horizontal basin before interacting with a ramp orientated perpendicular to flow direction. The incoming flow parameters remained constant, whilst the slope angle was independently varied. On a 20° slope, superelevation of the flow and flow stripping of the upper, dilute region of the flow occurred high on the slope surface. This resulted in a strongly divergent flow and the generation of complex multidirectional flows (i.e. combined flows). The superelevation and extent of flow stripping decreased as the slope angle increased. At 30° and 40°, flow reflection and deflection, respectively, are the dominant flow process at the base of slope, with the reflected or deflected flow interacting with the parental flow, and generating combined flows. Thus, complicated patterns of flow direction and behaviour are documented even on encountering simple, planar topographies orientated perpendicular to flow direction. Combined flows in deep-water settings have been linked to the interaction of turbidity currents with topography and the formation of internal waves with a dominant oscillatory flow component. Here, combined flow occurs in the absence of an oscillatory flow component. A new process model for the formation and distribution of hummock-like bedforms in deep-marine systems is introduced. This bedform model is coupled to a new understanding of the mechanics of onlap styles (draping versus abrupt pinchout) to produce a spatial model of gravity-current interaction, and deposition, on slopes to support palaeogeographical reconstructions.

Keywords Combined flows, flow confinement, flume experiments, hummocky bedforms, low-density turbidity currents, onlap styles, orthogonal topography.

INTRODUCTION

Turbidity currents are the principal mechanism for sediment transfer from shallow-water to deep-water environments (Kuenen & Migliorini, 1950; Middleton & Hampton, 1973; Simpson, 1997), resulting in the largest accumulations of sediment on Earth (Curry & Moore, 1971; Emmel & Curry, 1983). Seafloor topography, which acts as a first order control on turbidity current behaviour, may be generated by depositional relief associated with mass transport deposits (e.g. Armitage *et al.*, 2009; Martínez-Doñate *et al.*, 2021; Allen *et al.*, 2022), levées and lobes (e.g. Groenenberg *et al.*, 2010; Kane & Hodgson, 2011), folds and faults (e.g. Haughton, 2000; Hodgson & Haughton, 2004; Cullen *et al.*, 2019), salt and mud diapirism (e.g. Kneller & McCaffrey, 1995; Toniolo *et al.*, 2006; Cumberpatch *et al.*, 2021; Howlett *et al.*, 2021), seamounts (e.g. Seabrook *et al.*, 2023) and abyssal plain mountains (e.g. Harris *et al.*, 2014).

Turbidity current behaviour is strongly influenced by the flow characteristics (i.e. velocity, thickness, concentration) and the nature of the seabed topography (i.e. gradient, form, substrate) (e.g. Kneller *et al.*, 1991; Edwards *et al.*, 1994; Patacci *et al.*, 2015; Tinterri *et al.*, 2016, 2022; Dorrell *et al.*, 2018a; Soutter *et al.*, 2021). Turbidity currents can be reflected, deflected and/or ponded, generating spatial variations in flow competence and capacity, and hence the loci of deposition and depositional character (Allen, 1991; Hiscott, 1994; Kneller & McCaffrey, 1995, 1999). Recent technological advances have enabled direct velocity measurements of natural turbidity currents, and estimations of their concentration; however, these measurements have solely been acquired in submarine canyons or channels (e.g. Talling *et al.*, 2023, and references therein). To date, no such measurements have been made where unconfined flows interact with seafloor topography, although palaeocurrent records from deposits show that complicated flow fields are established (e.g. Pickering & Hiscott, 1985; Kneller *et al.*, 1991; Hodgson & Haughton, 2004).

The superimposition of unidirectional, and multidirectional and/or oscillatory flow components (i.e. combined flows), produces distinctive bedforms with a high degree of spatial and morphological variability (Clifton, 1976). Such bedforms include hummocky cross-stratification (HCS) (e.g. Arnott & Southard, 1990; Duke *et al.*, 1991; Dumas & Arnott, 2006; Wu *et al.*, 2024)

and sigmoidal cross-lamination in small-scale and large-scale ripples (e.g. Yokokawa, 1995; Dumas & Arnott, 2006; Tinterri, 2006, 2007). Hummock-like structures, large asymmetrical ripples, biconvex ripples and symmetrical megaripples have been documented in several deep-water systems (e.g. Privat *et al.*, 2021, 2024; Tinterri *et al.*, 2022; Martínez-Doñate *et al.*, 2023; Siwek *et al.*, 2023; Taylor *et al.*, 2024), and are typically postulated to have formed as a result of the generation of combined flows (cf. Mulder *et al.*, 2009). However, the combined flow paradigm in deep-water systems is based upon two-dimensional experimental observations.

Observations from 2D experiments of turbidity currents rebounding against topographic slopes (e.g. Pantin & Leeder, 1987; Edwards *et al.*, 1994; Kneller & McCaffrey, 1995; Kneller *et al.*, 1997) have been used to support outcrop-based models for the formation of combined flows and the formation of hummock-like structures in deep-water systems (Fig. 1) (e.g. Tinterri, 2011; Tinterri *et al.*, 2016, 2022; Privat *et al.*, 2021, 2024; Martínez-Doñate *et al.*, 2023). Tinterri (2011) suggests that flow transformations following the deceleration of flows upon incidence with slopes produce a hydraulic jump, akin to bores described semi-quantitatively with time-lapse photography and particle tracking by Edwards *et al.* (1994). It is hypothesized that the superimposition of the subcritical, unidirectional turbidity current, and an oscillatory flow component from the internal waves generated by supercritical upstream-migrating bores, produces combined flow in density currents (Tinterri, 2011; Tinterri *et al.*, 2016). Whether the same mechanisms for combined flow generation are active following the interaction of 3D, unconfined density currents with planar containing topography has not been explored experimentally. Understanding the flow process interactions of unconfined low-density gravity currents with orthogonal containing slopes is therefore crucial for interpreting turbidity current evolution and onlap geometries, and bedform and facies variability in 3D space on slopes.

Although previous physical experiments have varied flow parameters and topographic configuration to examine turbidity current flow dynamics and deposits (e.g. Kneller *et al.*, 1991, 1997; Edwards *et al.*, 1994; Amy *et al.*, 2004; Brunt *et al.*, 2004; Patacci *et al.*, 2015; Howlett *et al.*, 2019; Reece *et al.*, 2024) only one has investigated the interaction of 3D, unconfined gravity

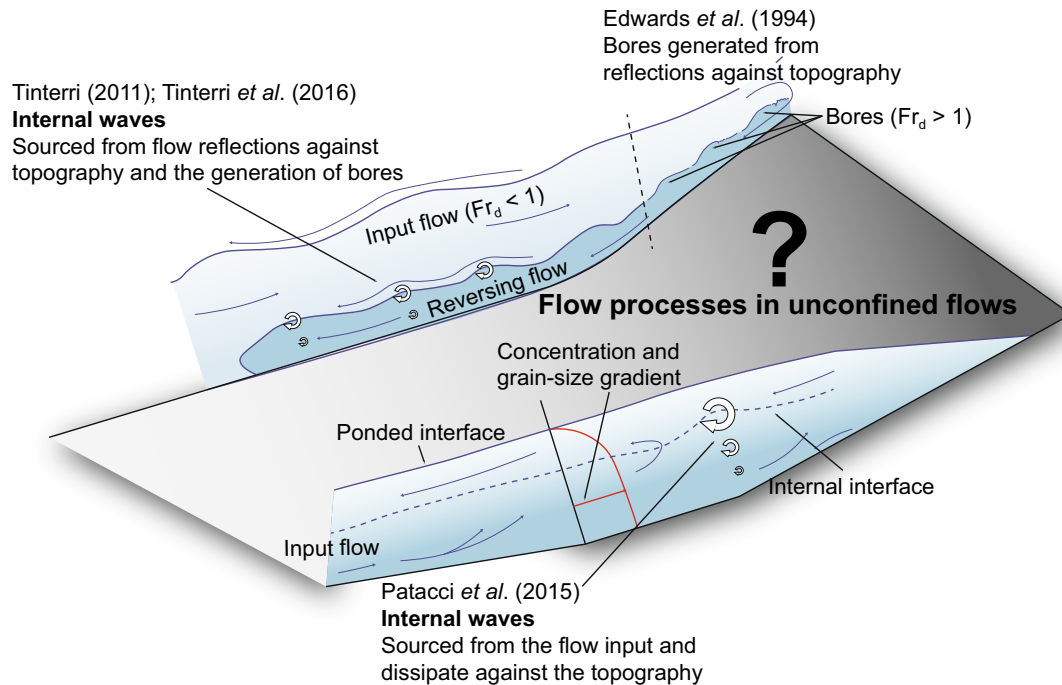


Fig. 1. Schematic diagram of existing models proposed for the generation of internal waves in turbidity currents. The generation of internal waves in ponded turbidity currents in two-dimensional experimental conditions was demonstrated by Patacci *et al.* (2015). Tinterri (2011) and Tinterri *et al.* (2016) derived their model from outcrop following flow reflections against topography, based on observations by Edwards *et al.* (1994) on the generation of bores. The question mark indicates the existing uncertainty in unconfined (three-dimensional) flow process behaviour. Fr_d , densimetric Froude number.

currents with simple, planar topographic slopes (Soutter *et al.*, 2021). Soutter *et al.* (2021) explored the depositional patterns around erodible basinal topography. With the basinal topography positioned orthogonal (90°) to the primary flow direction, and with sediment-laden gravity flows (17% by volume concentration), the denser material within the flow was observed to onlap the base of the containing slope, whereas the low density, finer grained material bypassed down-dip as it surmounted the topographic barrier (Soutter *et al.*, 2021). Notably, the high concentration sediment gravity flows and steep angle of the experimental platform (11°) produced gravity currents on the slope and the proximal basin floor of the flume tank, upstream of the topographic barrier, with basal 'slip-velocities' (i.e. the streamwise velocity measured at the base of the flow is not zero). This suggests that the sediment gravity flows of Soutter *et al.* (2021) are more akin to grain-flows and debris-flows (*sensu* Méjean *et al.*, 2022).

In contrast, the experiments herein, are low-density, fully-turbulent, gravity currents that were unable to surmount the containing topographic slope. This experimental configuration permits observations of unconfined gravity current dynamics and evolution both at the base of, and on, the slope surface, which has not been previously explored. The influence of the topographic containment on flow processes is expressed by the topographic containment factor (h'), where $h' = h/h_{\max}$, and h is flow height and h_{\max} is the maximum run-up height. The containment factor increases as the slope angle increases from 20° to 30° to 40° . Increasing the slope angle affects the degree of flow stripping, and the velocity structure and evolution on the slope surface and at the base of the slope.

The aim of the current study is to document the interaction between scaled, unconfined saline density currents and partially containing orthogonal topography using 3D flume tank experiments. The objectives are to: (i) assess

how the angle of the containing frontal topography (independently varied at 20°, 30° and 40°) affects density current evolution and the generation of combined flows; (ii) investigate how the mechanisms of flow reflection and deflection, and the novel observation of flow divergence, operate on the slope surface and influence interactions with the incoming flow at the base of the slope in unconfined settings; and (iii) discuss the effect of combined flows on the deposit character and onlap geometry in deep-water settings.

METHODS

Experimental set-up

Experiments were performed in the Sorby Environmental Fluid Dynamics Laboratory, University of Leeds, UK, using a 10 m long, 2.5 m wide and 1 m deep flume tank (Fig. 2A and B). A 1400 l saline solution (2.5% excess density) was prepared in a 2000 l mixing tank. The saline solution was pumped (using an inverter controlled centrifugal pump) into the main tank through an inlet pipe centred on the experimental platform and into a straight-sided 0.62 m long, 0.26 m wide channel, before the flow debouched into the main tank. The main tank and inlet channel were both set on a horizontal basin floor (i.e. 0° slope angle). The main tank was filled with tap water to a depth of 0.6 m. The pump speed was manually adjusted when the flow rate deviated from the reference value of 3.6 l s^{-1} . The flow rate variability was accurate to $\pm 0.05 \text{ l s}^{-1}$ of the reference value throughout the duration of the experiment (<2% error) (Table 1).

Unconfined flow properties

Three initial experiments were performed without any containing topography. Firstly, the unconfined flow was visualized for the full duration of the experiment through the free-water surface, using an overhead camera above the flume tank (Video 1). Fluorescent tracer dye was used to aid visualization of the flow. Measurements of the flow were recorded along the tank axis, at 3 m downstream of the channel mouth, to provide a base case for comparison with the flows interacting with the containing topography (Fig. 3A and B; Table 2). An Ultrasonic velocimeter Doppler profiler (UVP

(Met-Flow, UVP DUO, 4 MHz, Met-Flow SA, Lausanne, Switzerland) was used to record the instantaneous downstream flow velocity (Fig. 4A and B). The UVP recorded the multiplexed velocity output from a vertically stacked array of 10 transducers from the entire flow height (see Table 2 for details of UVP parameters). Positive values of streamwise velocity are measured as the flow travels into the basin (Fig. 3A). A Nortek Vectrino Acoustic Doppler velocity profiler (ADV) (Nortek Group, Rud, Norway) was used to record the instantaneous flow velocities of the unconfined flow at 3 m downstream of the channel mouth, before the flow interacted with the slope. Where the ADV was used, positive streamwise velocities are measured as the flow travels towards the slope, whereas negative values record flow reversal. Additionally, for the ADV data (Fig. 3B), positive and negative values of cross-stream velocity data correspond to left-lateral and right-lateral movement of the flow, respectively, while positive and negative values of vertical velocity data correspond to the up – and down – movement of the flow, respectively. Such cross-stream and vertical data are not available from the UVP, which measures streamwise velocity only. Flow density was also measured (Fig. 4G and H), using an array of 12 syphons, and also for two additional experiments performed with frontally containing topography (Fig. 4I). Syphon sampling was initiated 5 s after the head passed, and lasted for 30 s. Twelve stacked syphons with 5 mm diameter tubing were deployed over a 0.095 m height, with the lowermost syphon 0.005 m above the base of the tank floor (Fig. 4G). The syphon array was connected to a peristaltic pump set to a constant withdrawal rate. The fluid was collected in sample pots and the density was measured using an Anton Paar DMA 35 portable densitometer (Anton Paar GmbH, Graz, Austria), with a resolution of 0.1 kg m^{-3} . The density was measured at a background temperature of 12°C, where the ambient density of water is 999.58 kg m^{-3} .

Froude scaling

Calculations of the Reynolds number (Re) and densimetric Froude number (Fr_d), permit the Froude scaling of experimental saline density currents with natural turbidity currents (Yalin, 1971) (see Table S1). Here, the measured parameters of the unconfined flow 3 m downstream of the channel mouth were used. The measurements were initiated 5 s after the head

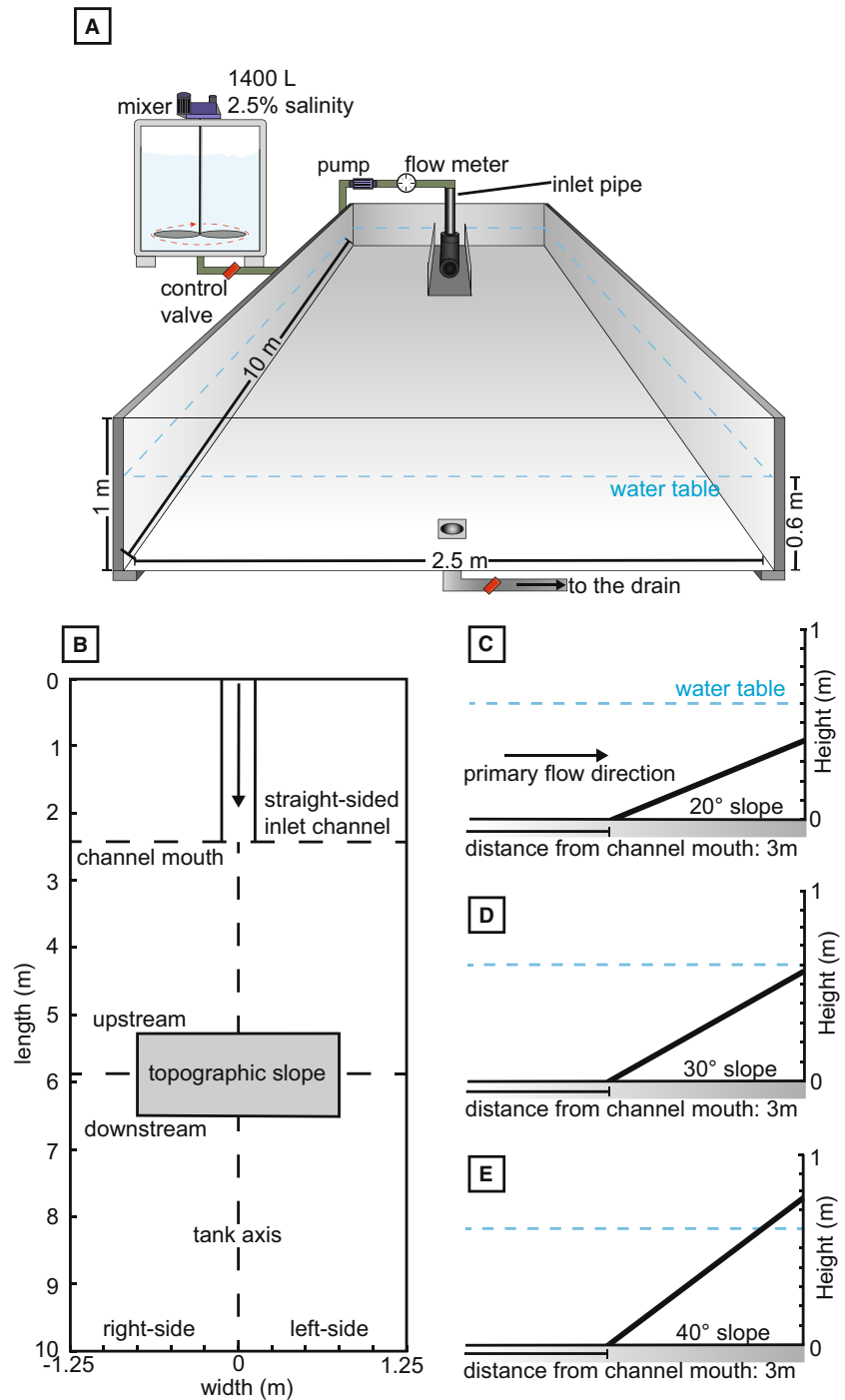


Fig. 2. (A) Flume tank and mixing tank configuration. (B) Plan view of flume tank and slope position. Right-side and left-side is with respect to the primary flow direction. (C) to (E) Configurations of the 20°, 30° and 40° topographic slopes.

passed, and lasted for 30 s. Froude scale modelling considers the Reynolds number (Re) relaxed compared to natural systems, but still within the fully turbulent regime, whereas the densimetric Froude number (Fr_d) is held as similar (e.g. Graf, 1971; Peakall *et al.*, 1996). In this study, the Reynolds number is taken to be:

$$Re = \frac{p_s U h}{\mu} \quad (1)$$

where p_s is the depth-averaged density of the gravity flow measured using the density syphon array, U is mean depth-averaged velocity, μ is dynamic viscosity, and h is the height at which

Table 1. Experimental configuration and data instrumentation [Ultrasonic Doppler velocity profiler (UVP), Acoustic Doppler velocity profiler (ADV) and density syphon] positions for all experiments. The instrumentation was placed along the tank axis. Unconfined-b and Unconfined-c: each instrument was positioned 3 m downstream of the channel mouth. For the experiments with the topographic slope, the slope was positioned 3 m downstream of the channel mouth and perpendicular to the primary flow direction. The reference values for mean flow rate (l s^{-1}) and the excess density of the input current (%) were 3.6 l s^{-1} and 2.5%, respectively.

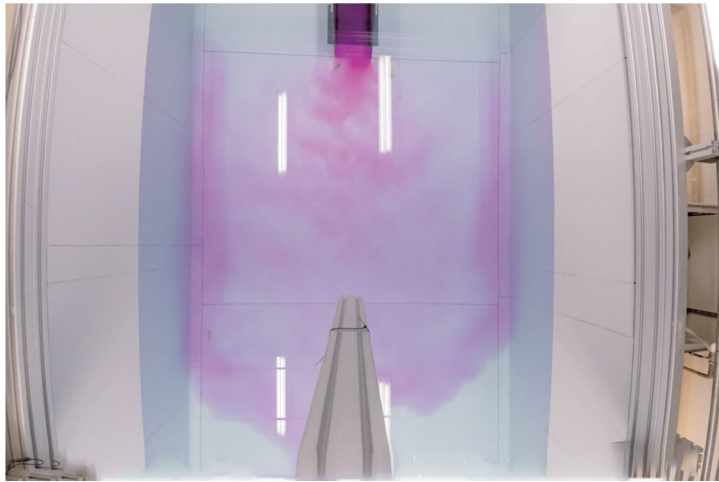
| Run | Slope angle ($^{\circ}$) | Instrumentation [height upslope (m)] | Mean flow rate (l s^{-1}) | Input current density (%) |
|--------------|----------------------------|--------------------------------------|--------------------------------------|---------------------------|
| Unconfined-a | – | Visualization | 3.61 | 2.50 |
| Unconfined-b | – | UVP | 3.60 | 2.50 |
| Unconfined-c | – | Density syphon | 3.60 | 2.50 |
| FC-20a | 20 | ADV (0) | 3.61 | 2.50 |
| FC-20b | 20 | ADV (0.10) | 3.60 | 2.49 |
| FC-20c | 20 | ADV (0.15) | 3.61 | 2.50 |
| FC-20d | 20 | Visualization | 3.60 | 2.51 |
| FC-20e | 20 | Density syphon (0) | 3.60 | 2.50 |
| FC-20f | 20 | Density syphon (0.10) | 3.60 | 2.50 |
| FC-30a | 30 | ADV (base) | 3.59 | 2.49 |
| FC-30b | 30 | ADV (0.10) | 3.60 | 2.50 |
| FC-30c | 30 | ADV (0.20) | 3.59 | 2.49 |
| FC-30d | 30 | Visualization | 3.59 | 2.49 |
| FC-40a | 40 | ADV (0) | 3.59 | 2.49 |
| FC-40b | 40 | ADV (0.08) | 3.59 | 2.50 |
| FC-40c | 40 | ADV (0.14) | 3.60 | 2.49 |
| FC-40d | 40 | Visualization | 3.58 | 2.50 |

the streamwise velocity recorded by the UVP reaches zero at the top of the flow. The depth-averaged density and velocity values are calculated by taking measurements at regularly-spaced intervals (0.05 m) from the profiles in Fig. 3A, for the velocity over the full depth of the flow recorded by the UVP, and for the density over the available depth profile and extrapolated points at the base and top of the flow (Fig. 3A). The flow height was 0.11 m.

The Reynolds number is used as an indicator of turbulence, where $Re > 2000$ represents a fully-turbulent flow (Simpson, 1997). Based on the unconfined reference experiments, the modelled flow had a Reynolds number of 3203 ($Re = 3203$), 3 m downstream of the channel mouth (i.e. a fully turbulent flow).

The Froude number (Fr) describes the ratio of inertial to gravitational forces for stratified flows. To indicate which of these forces is dominant, flows of $Fr > 1$ are termed supercritical, while flows of $Fr < 1$ are termed subcritical (Ellison & Turner, 1959). Hydraulic jumps occur when flows transition from supercritical to subcritical, here the critical Froude number (Fr_c), is denoted by $Fr_c = 1$, although this can vary in strongly stratified density currents (e.g. Sumner *et al.*, 2013; Cartigny *et al.*, 2014). For turbidity currents, the densimetric Froude number (Fr_d) is used to account for the reduced gravity (g') derived from the density difference between the flow and the ambient fluid (Kneller & Buckee, 2000):

$$Fr_d = U / \sqrt{g'h} \quad (2)$$



Video 1: Time-lapse video of the evolution of the unconfined density current throughout the experimental run (3× playback speed). The field of view is the full width of the tank (2.5 m). To aid flow visualization, the input flow is dyed with fluorescent, purple tracer dye. The flow is observed to exit from the channel at the channel mouth and begins to radially expand into the basin. At 3 m from the channel mouth, the incoming head of the flow is unconfined. For the subsequent experiments with the orthogonal slope, the leading edge of the base of slope was positioned at 3 m from the channel mouth.

$$g' = g(p_s - p_a) / p_a \quad (3)$$

where g is acceleration due to gravity, and p_a is the density of the ambient fluid, measured at 12°C. [Correction added on 15 November, after first online publication: rho subscript 's' at the end of Equation 3 has been corrected to rho subscript 'a'.]

Based on the unconfined reference experiments, the modelled flow had a densimetric Froude number of 0.50 ($Fr_d = 0.50$) (i.e. a sub-critical flow). This value, and the visually-observed hydraulic jump following debouching of the flow at the channel mouth, may be considered analogous to basin floor flows that have passed through the channel-lobe transition zone, experiencing a loss in flow confinement (e.g. Komar, 1971; Hodgson *et al.*, 2022).

Containing topography

The topography was created using a linear, non-erodible slope. The 1.5 m wide planar slope, not spanning the full width of the 2.5 m wide flume tank, was positioned orthogonal (90°) to the primary flow direction and across the tank axis, 3 m downstream of the channel mouth (Fig. 2B). The angle was independently varied at 20°, 30° and 40° (Fig. 2C to E). The slope had a bevelled leading

edge, thus minimizing the step at the base of slope. For the 20°, 30° and 40° slope configurations the maximum height of the slope was 0.410, 0.585 and 0.760 m, respectively. The containment factor (h') value for all three slope configurations describes a flow unable to surmount the containing topographic slope (Fig. 5). Due to the width of the slope (1.5 m) compared to the width of the tank (2.5 m), the flow is partially-contained.

The use of 20°, 30° and 40° slope angles herein is motivated by outcrop examples of onlap angles, previous experimental models and the water depth of the experimental basin. The modelled flows herein are more dilute than in previous experiments on topographic interaction of density currents (e.g. Pantin & Leeder, 1987; Kneller *et al.*, 1991; Edwards *et al.*, 1994; Kneller, 1995; Patacci *et al.*, 2015), making them more mobile upslope. This, coupled with the maximum water depth of the flume tank (0.6 m), meant that slope angles less than 20° were difficult to achieve without the flow surmounting the topographic slope or the flow travelling upslope and interacting with the free-water surface. Examples of similar slope angles used in previous experimental studies, include: 20° (Kneller *et al.*, 1991), 25° ± 5° (Soutter *et al.*, 2021), 28° (Muck and Underwood, 1990) and 30° (Kneller, 1995). In Annot, France, the basin

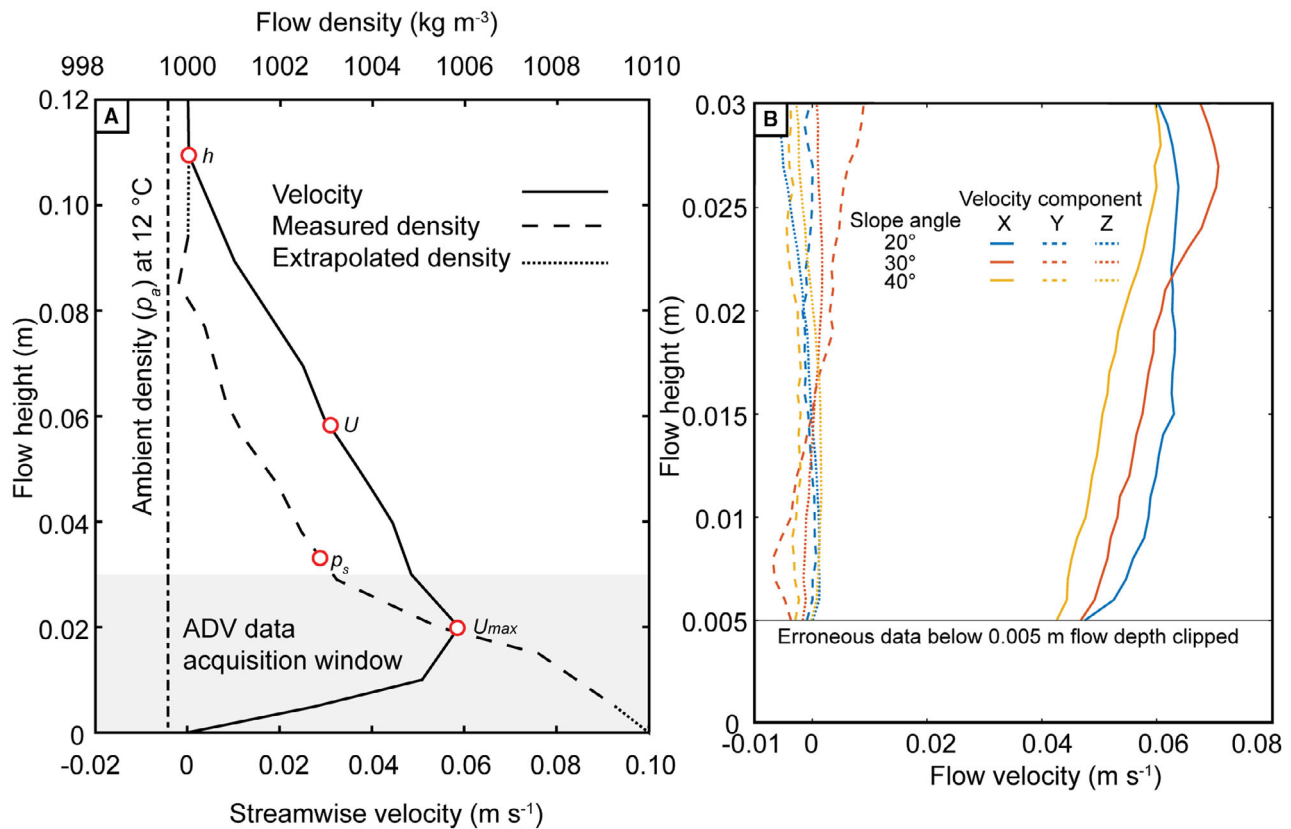


Fig. 3. Comparative velocity profiles measured along the tank axis, 3 m downstream of the channel mouth. (A) Time-averaged streamwise velocity [using the Ultrasonic Doppler velocity profiler (UVP)] and density profiles of the unconfined flow. Both measurements were initiated 5 s after the head passed, and lasted for 30 s. U_{max} , U and h denote the maximum streamwise velocity, depth-averaged streamwise velocity and flow height, respectively. For the density profile, p_s is the depth-averaged density. The dashed line indicates the measured density data, and the dotted line is density data extrapolated below 0.05 m flow depth and above 0.09 m flow depth. The density of the ambient water (p_a) as measured at a background temperature of 12 °C, where the ambient density of water is 999.6 kg m⁻³. (B) 5 s time-averaged velocity profiles [using the Acoustic Doppler velocity profiler (ADV)] measured from the first 5 s from the head of the flow at the 3 m position (base of slope), prior to the collapse of the flow downslope. The three components of measured velocity, i.e. streamwise (X), cross-stream (Y) and vertical (Z) are indicated.

margin slope angle is between 10° and 30° (Sinclair, 1994; Hilton and Pickering, 1995; Joseph *et al.*, 2000; Puigdefàbregas *et al.*, 2004; Smith and Joseph, 2004; Tomasso and Sinclair, 2004; Soutter *et al.*, 2019). Locally steep topography is common in deep-water settings, for example, related to fault scarps (e.g. Haughton, 1994; Hodgson & Haughton, 2004; Bakke *et al.*, 2013) and mass-transport deposits (e.g. Martínez-Doña *et al.*, 2021; Allen *et al.*, 2022). That being said, slope angles less than 10° are common in many basins (e.g. Bakke *et al.*, 2013; Spychala *et al.*, 2017), and the implications of this work for lower angle slopes are discussed later.

An initial experiment was performed using a series of GoPro Hero 10 Black cameras (GoPro, Inc., San Mateo, CA, USA) to visualize the flow at each topographic configuration. Fluorescent tracer dye was injected through a series of tubes (5 mm in diameter) onto the slope surface to aid visualization (Videos 2–4). The dye injection tubes were inserted into an array of evenly-spaced drilled holes and were flush with the slope surface, thus minimizing any surface irregularities. The rate of dye injection was controlled using a peristaltic pump, set to a constant discharge rate for all experimental runs. The net input of fluid into the tank will lead to

Table 2. Parameters for the Ultrasonic Doppler velocity profiler (UVP) and Acoustic Doppler velocity profiler (ADV) used in the current study. UVP is used to quantify instantaneous flow velocities of the unconfined flow, measured 3 m downstream of the channel mouth and along the tank axis. ADV is used to measure the instantaneous flow velocities 3 m downstream of the channel mouth along the tank axis, at the base of each slope configuration and two positions on each slope surface.

| UVP parameters | | ADV parameters | |
|-----------------------------------|-----------------------------------|--------------------------------|------------------------------|
| Instrument name | Met-flow UVP monitor 4 | Instrument name | Vectrino doppler velocimeter |
| Sampling frequency | 4 Hz | Sampling frequency | 100 Hz |
| Probe height above tank floor | 1, 2, 3, 4, 5, 6, 7, 9, 11, 13 cm | Speed of sound in water | 1465 m s ⁻¹ |
| Velocity of ultrasound in water | 1480 m s ⁻¹ | Number of transducers | 4 |
| Number of bins | 128 | Number of cells | 31 |
| Number of profiles per transducer | 1000 | Cell start below head of probe | 40 mm |
| Sampling period | 11 ms | Cell end below head of probe | 70 mm |
| Velocity range | 256 mm s ⁻¹ | Cell size | 1 mm |
| Minimum velocity | -128 mm s ⁻¹ | Velocity range (streamwise) | 500 mm s ⁻¹ |
| Maximum velocity | 128 mm s ⁻¹ | Horizontal velocity range | 497 mm s ⁻¹ |
| Minimum measurement distance | 4.99 mm | Vertical velocity range | 130 mm s ⁻¹ |
| Maximum measurement distance | 99.71 mm | Instrument run time | 240 s |

a diffuse compensatory return flow in the upper part of the water column, however this could not be visually observed, and the orthogonal orientation of the slope stops any return flow from directly affecting the experiments. For each slope configuration, three subsequent runs with an ADV were performed to quantify the instantaneous three-dimensional flow velocities, at a frequency of 100 Hz (see Table 2 for details of ADV parameters). The ADV can measure 30 measurement points with three component velocities (downstream and cross-stream components, X and Y, respectively, and two measurements of the vertical component, Z1 and Z2, associated with the X and Y receivers of the ADV probe, respectively) over a depth range of 0.03 m. The measurement zone starts 0.04 m below the probe head, and with the basal measurement recorded at the interface of the tank floor and the slope (Fig. 4C to F). The five lowermost ADV measurement points were clipped from all experimental runs due to excessive data noise resulting from signal interferences with the floor/slope. The ADV was positioned along the tank axis, at

the base of each slope configuration to quantify the instantaneous velocities of the flow interacting with the topographic slope. The position of the ADV on the slope surface was dependent on the slope angle and determined with the aid of the flow visualization videos (see Table 1 for ADV positions). For the experiments performed with the UVP and ADV, the saline density currents were seeded with neutrally-buoyant, hollow glass microspheres (Spherical 110-P8) (Potters Industries, Malvern, PA, USA) to provide an acoustic contrast to the flow, which produces the white colour to the flows observed in Videos 2–4. The lowermost ADV was located at the approximate height upslope at which a stable flow front developed. The uppermost position was located where the flow height was approximately 0.07 m thick; at flow thicknesses below 0.07 m, the precision of the ADV data measurement window is not considered accurate enough. All instantaneous velocity data recorded by the UVP and ADV were post-processed to remove any data spikes more than two standard deviations away from the mean and replaced with

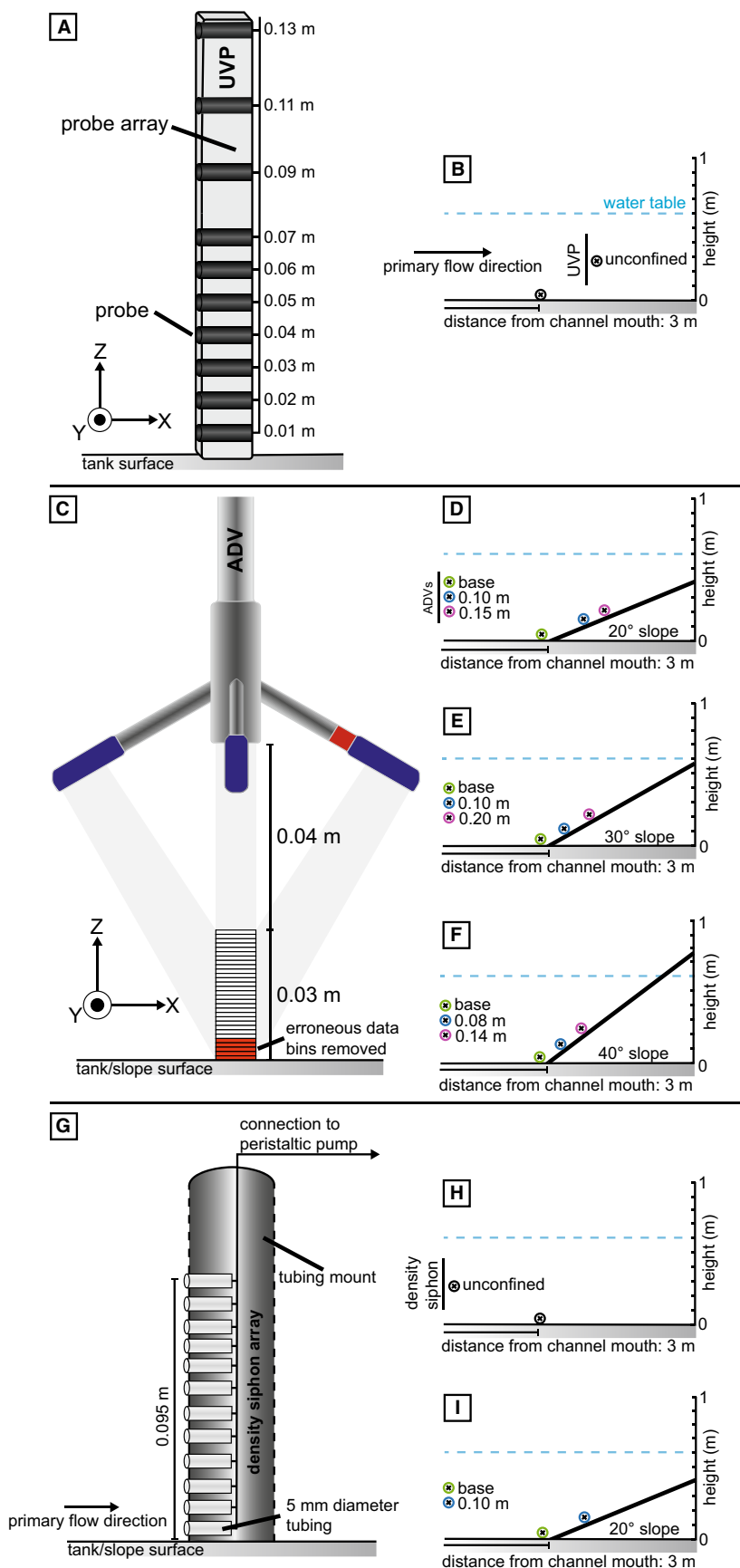
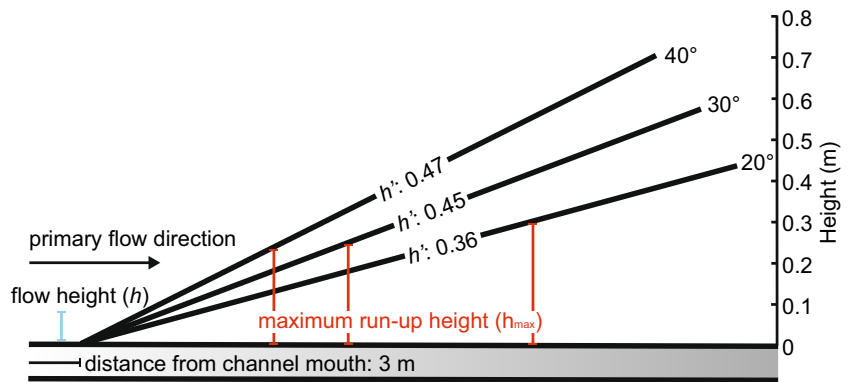


Fig. 4. (A) Schematic diagram of the Ultrasonic Doppler velocity profiler (UVP), with the probe heights annotated. (B) Configuration of the UVP used to quantify the velocity of the unconfined density current. (C) Schematic diagram of the Acoustic Doppler velocity profiler (ADV). The basal 0.03 m is the data acquisition window of the ADV instrument. (D), (E) and (F) Configuration for the 20°, 30° and 40° slopes, respectively, with the three ADV positions annotated. For (A) and (C), X, Y and Z are with respect to the velocity components. (G) Schematic diagram of the density syphon array. The syphon array was connected to a peristaltic pump set to a constant withdrawal rate to measure the density of the flow for the duration of the experiment. (H) and (I) Configuration of the syphon array used to quantify the density of the unconfined flow and for the 20° slope.

Fig. 5. Containment factor (h') for each slope configuration ($h' = h/h_{\max}$), where h = flow height (0.11 m) and h_{\max} = maximum run-up height. The observed h_{\max} for the 20°, 30° and 40° slopes is 0.30 m, 0.24 m and 0.23 m, respectively. For all experimental configurations, the incoming flow was unable to surmount the containing topographic slope.



Video 2: Annotated real-time video illustrating the temporal evolution of the flow with a 20° slope. Fluorescent dye injected at a series of lateral points onto the slope surface was used to visualize the interaction of the density current and the containing topography. Gridded white lines were marked on the slope surface to aid the identification of the height at which the stable flow front developed and the maximum run-up height (h_{\max}).

an 11-point moving average (see Buckee *et al.*, 2001; Keevil *et al.*, 2006).

RESULTS

Unconfined flow

Velocity and density structure

The flow measured at 3 m downstream of the channel mouth is quasi-steady, with a radially spreading front (Video 1). Both the UVP velocity and density measurements of the unconfined flow were initiated 5 s after the head passed, and lasted for 30 s (Fig. 3A). The time-averaged streamwise velocity recorded by the UVP

(Fig. 3A) gives a maximum streamwise velocity (U_{\max}) of 0.059 m s^{-1} , at a height of 0.02 m (Fig. 3A). The flow height is 0.11 m, and the mean depth-averaged streamwise flow velocity is 0.029 m s^{-1} (Fig. 3A). Prior to the interaction of the unconfined flow with the slope, the ADV measured the three components of velocity for the incoming front of the head of the current, over a 5 s period. The U_{\max} of the incoming flow is $0.065 \pm 0.005 \text{ m s}^{-1}$ (Fig. 3B); albeit the height over which the ADV measures may not quite capture the U_{\max} position in the 40° case (see unbroken yellow velocity profile in Fig. 3B), and thus may be an underestimate. Over the 5 s window in which it was recording the unconfined flow velocity, the ADV measured the cross-

stream velocity component as -9 to 12% of the maximum streamwise velocity, and the vertical velocity component ranges as -9 to 2% of the maximum streamwise velocity (Fig. 3B). The flow is well-stratified at a distance of 3 m downstream of the channel mouth (Fig. 6B). The dense, basal region of the flow (0.03 m thick) is separated from the dilute, upper region of the flow (0.06 m thick) by a distinct density interface (Figs 3A and 6B). The density of the flow decreases upward from 1009 kg m^{-3} (0.9% excess density) in the basal region of the flow to 1000 kg m^{-3} at 0.09 m flow height (Fig. 3A).

Flow interactions with containing topography

The distance downstream from the channel mouth to the containing topography (3 m) and input flow parameters were uniform for all experimental runs. The slope was positioned orthogonal to the primary flow direction, with the slope angle independently varied at 20° , 30° and 40° . Comparing how changes in slope angle affect the flow velocity and density structure, and evolution, provides a better understanding of processes active at the base of, and on, the slope surface. The flow visualization (Videos 2–4; Figs 7 and 11) permits qualitative observations of the flow processes across the width of the slope surface and at the base of slope, while, at a quantitative level, the ADV (Figs 8, 9, 10, 12 and 13) and density (Fig. 6B to D) measurements provide data on the central axis of the flow.

Lateral flow spreading on the slope surface

Upon incidence with the containing topography, the flow visualization videos show that the superelevation of the flows, and the nature of the radially spreading front, differ as a function of slope angle (Videos 2–4; Fig. 7). At 20° , the flow continues to spread radially on the slope surface, diverging away from its central streamline, with a high degree of spreading towards the lateral edges of the slope (Video 2). At 20° , h_{max} occurs along the flow axis, approximately 0.30 m upslope, 2.73 times the flow height (Video 2; Fig. 7A). The initial degree of lateral flow spreading on the 30° slope is like that observed at 20° (Video 3). However, because of the increased containment at 30° , the component of flow reflection on the slope surface is enhanced, resulting in less lateral flow spreading (Video 3). At 30° , h_{max} occurs along the flow axis, approximately 0.24 m upslope, 2.19 times the flow height (Video 3; Fig. 7B). At 40° , the

radially spreading head decelerates rapidly at the base of slope and is deflected along the basal edge of the slope (Video 4). The enhanced topographic steering generated at 40° decreases the flow's upslope momentum compared with the 20° and 30° slopes, and hence decreases the degree of lateral flow spreading on the slope. At 40° , h_{max} occurs towards the lateral edges of the slope, approximately 0.23 m upslope, 2.10 times the flow height (Video 4; Fig. 7C).

Degree of flow thinning and stripping

The flow visualization from each slope configuration, shows that the flow thins as it decelerates upslope (Videos 2–4). Density measurements 3 m downstream show a well-stratified flow with a distinct interface between the dense, basal region and the dilute, upper region of the flow (Fig. 6B). The density measurements recorded at 0.1 m upslope of the 20° slope show that the dilute region of the flow decouples from the dense region of the incoming flow (Fig. 6D) and continues to thin upslope before reaching h_{max} (Video 2). The thinning and density decoupling of the flow is akin to the process of flow stripping (Piper & Normark, 1983). The zone of flow stripping that develops at each slope configuration is defined qualitatively (Fig. 6A), using the flow visualization (Videos 2–4), and supported quantitatively for the 20° slope using density measurements of the flow (Fig. 6C and D). The lower limit of the zone of flow stripping is demarcated by the height upslope at which the basal region of the flow reverses downslope (Videos 2–4), hence marking the onset of flow thinning upslope (termed 'height of initial flow reversal') (Fig. 6A). The upper limit of the zone of flow stripping is defined by h_{max} (Fig. 6A). Upon incidence with the 20° slope, the height of initial flow reversal occurs approximately 0.09 m upslope (Video 2). The dense region of the decelerating flow reverses downslope, causing the flow to thicken and mix as it interacts with the incoming flow at the base of slope, generating a non-stratified flow (Fig. 6C). The degree of flow thinning and zone of flow stripping generated on the 20° slope is enhanced compared to the 30° slope (Fig. 6A). At 30° , the initial flow reversal occurs approximately 0.13 m upslope (Video 3) and the zone of flow stripping extends to 0.24 m upslope (Fig. 6A). At 40° slope, the flow decelerates strongly at the base of slope and there is little decoupling observed between the dense region of the flow and the more dilute region of the flow on the slope surface (Video 4). The height of the

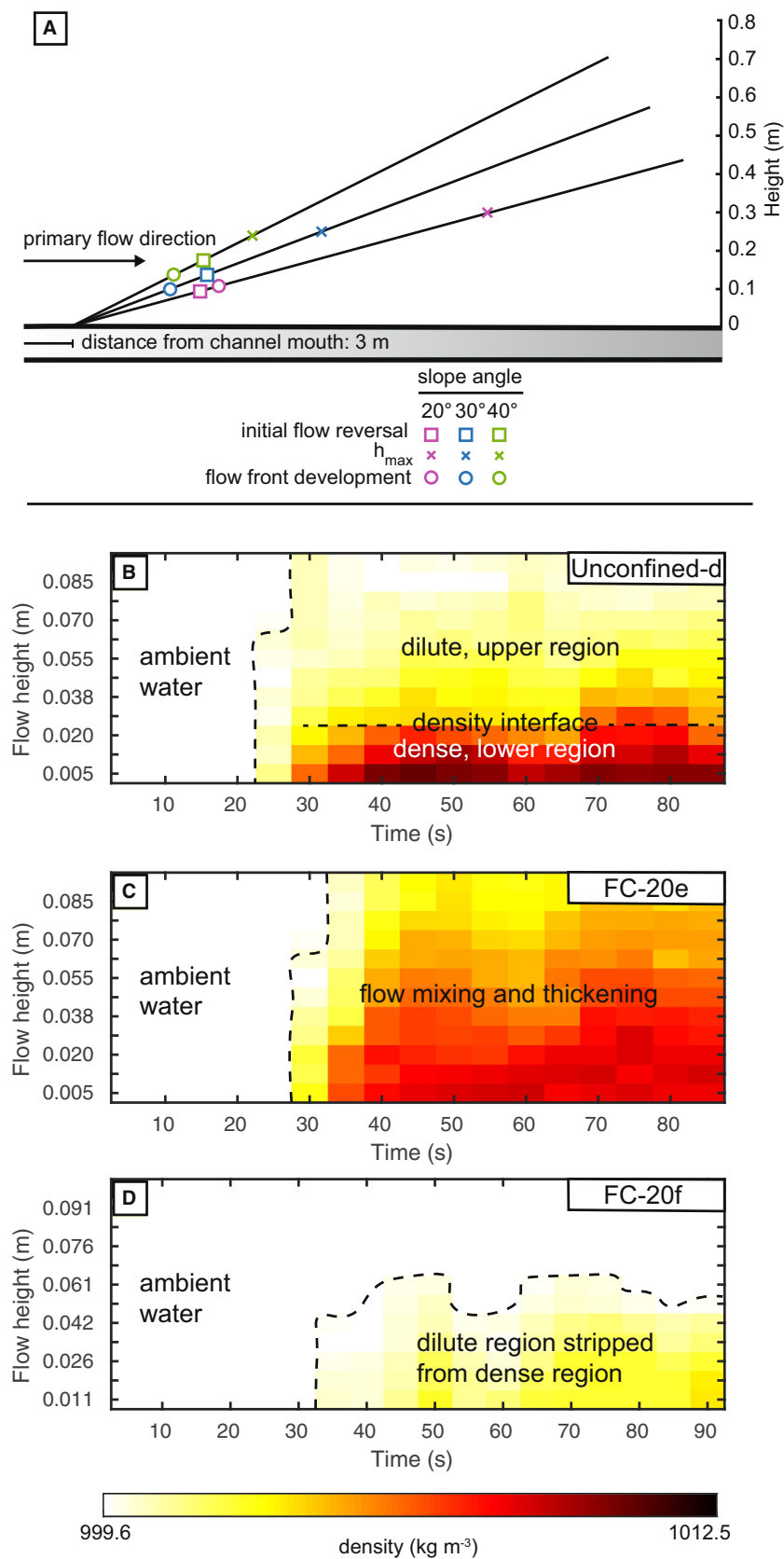


Fig. 6. (A) The extent of the zone of flow stripping that is generated on the slope surface for each topographic configuration. The lower limit of the zone of flow stripping is demarcated by the height of initial flow reversal. The upper limit is defined by the maximum run-up height (h_{\max}) of the flow. The extent of the zone of flow stripping decreases with an increasing containment factor (B), (C) and (D). Density time series of (B) the unconfined flow recorded at the same position as the base of slope in the topographic slope experiments, (C) at the base of the 20° slope (FC-20e) and (D) 0.1 m upslope (FC-20f) along the tank axis.

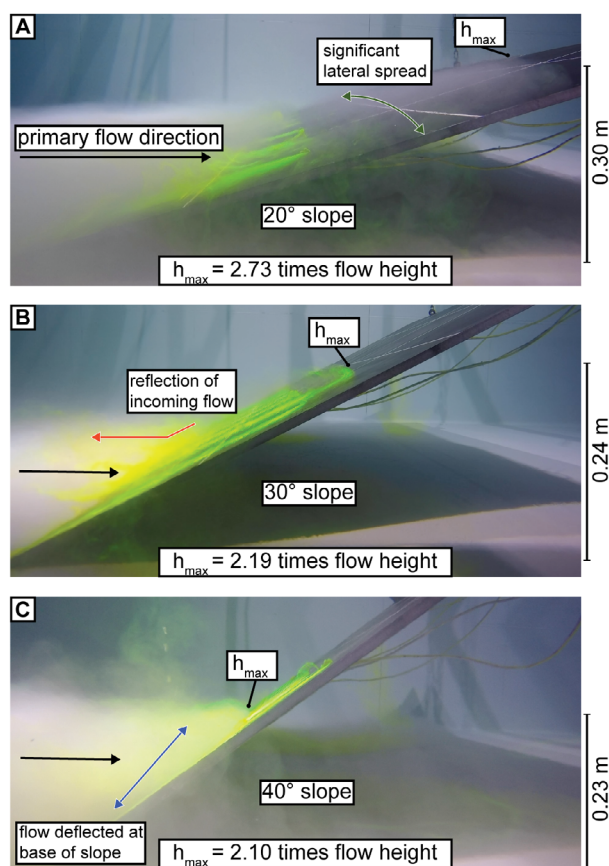


Fig. 7. Photographs captured using underwater cameras, with the maximum run-up height (h_{\max}) and degree of lateral flow spreading annotated. (A) 20° slope. (B) 30° slope. (C) 40° slope. Fluorescent dye is injected at a series of lateral points onto the slope surface using a peristaltic pump set at a constant flow rate, to aid in the visualization of the incoming flow interacting with the slope. The h_{\max} and degree of lateral flow spreading decreases as the angle of the slope, and hence the topographic containment factor, increases.

initial flow reversal in this 40° case is approximately 0.18 m, slightly higher than that on the 20° and 30° slopes. Despite this, the smaller h_{\max} value of approximately 0.23 m upslope led to a smaller zone of flow stripping (Fig. 6A). The degree of flow stripping and thinning strongly influences the character of the reversed flow at the base of slope.

Primary and secondary flow reversals

The first recorded negative streamwise velocity signal corresponds to the primary flow reversal (Figs 8, 9 and 10). The subsequent repeated fluctuations correspond to the secondary flow

reversals (Figs 8, 9 and 10). The flow visualization (Videos 2–4) and depth-constrained ADV velocity time-series data (Figs 8, 9 and 10) demonstrate how the magnitude of the primary flow reversal and the fluctuations of the secondary flow reversals are a function of slope angle. The magnitude of the primary flow reversal is characterized by the arrival time of the primary reversal at the base of the slope, the periodicity of the reversal, and its velocity signal.

On a slope of 20°, before the primary flow reversal is recorded at the base of slope, the parental flow decelerates due to the interaction with the weakly reversing flow as it travels downslope. The primary flow reversal occurs approximately 12 s after the parental flow initially arrived (Video 2), with a recorded streamwise velocity of approximately -0.03 m s^{-1} (Fig. 8C). The arrival of the primary flow reversal at the base of slope marks the onset of enhanced cross-stream velocity fluctuations as the two flow components interact (Fig. 8D). The primary flow reversal is recorded at the base of slope over a 9 s window (Fig. 8C). Before the parental flow re-establishes at the base of slope, a 4 s period of stasis, where the streamwise velocity is negligible (Fig. 8C), marks the period of the greatest cross-stream velocity variability (Fig. 8D). At 30°, there is limited deceleration of the parental flow at the base of slope before the primary flow reversal is recorded (Fig. 9C). The arrival of the primary flow reversal is recorded 6 s after the parental flow initially arrived at the base of slope (Fig. 9B), with a streamwise velocity of approximately -0.04 m s^{-1} (Fig. 9C). The interaction between the primary flow and the reversal generates an increased cross-stream velocity component at the base of slope (Fig. 9D). The primary flow reversal is maintained for approximately 10 s before the parental flow re-establishes (Video 3). At 30°, following the interaction of the primary flow reversal with the parental flow, the body of the density current appears to inflate, thickening for approximately 30 s, becoming flat-topped and subsequently propagating upstream of the topographic slope (Video 3). The highest degree of flow thickening is observed at the 30° slope (Video 3). At 20° and 40°, the inflated, flat-topped cloud generated at the base of slope is maintained for approximately 10 s and 20 s, respectively, before then propagating upstream of the topographic slope and dissipating throughout the experimental basin (Videos 2 and 4). Despite the propagation of the thickened cloud upstream, no soliton wave trains or bores were observed, as

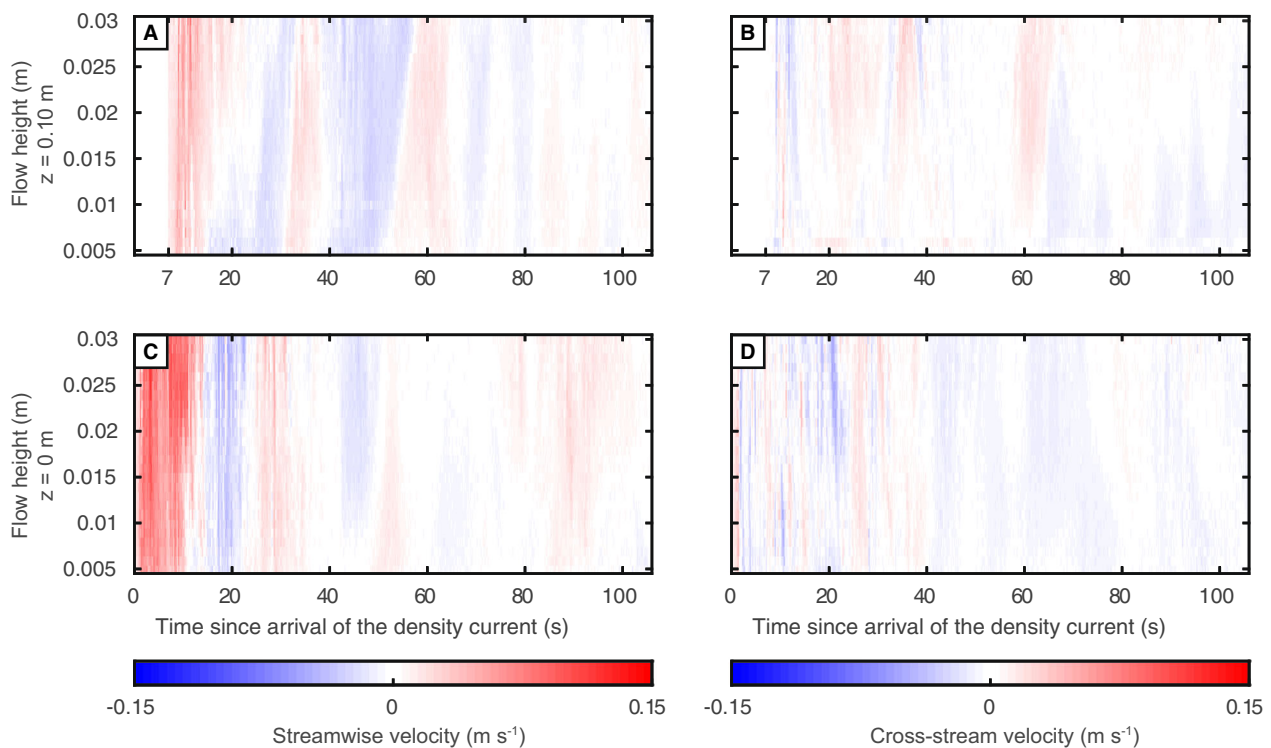


Fig. 8. Acoustic Doppler velocity profiler (ADV) velocity time series of saline density currents interacting with the 20° slope. (A) and (B) Streamwise and cross-stream velocity time series respectively ($z = 0.10$ m upslope). (C) and (D) Streamwise and cross-stream velocity time series respectively ($z = 0$ m, base of slope). The clipped data from the first 7 s in (A) and (B) represents the time taken for the flow to travel from the base of slope to 0.1 m upslope.

has been observed in more confined, 2D experiments (e.g. Pantin & Leeder, 1987; Edwards *et al.*, 1994; Kneller *et al.*, 1997). At 40°, the primary flow reversal arrives at the base of slope, approximately 12 s after the parental flow first arrived with a decreased streamwise velocity of approximately -0.02 m s^{-1} (Fig. 10C). The parental flow at the base of slope re-establishes approximately 7 s after the primary flow reversal was first recorded (Fig. 10C). There is negligible streamwise velocity variability in the basal 0.005 to 0.01 m of the flow during the primary flow reversal (from 12 to 17 s of Fig. 10C), whereas the cross-stream velocity component during the primary flow reversal operates over the full height of the data acquisition window, at approximately 0.03 m s^{-1} (Fig. 10D).

A quasi-stable flow front develops on the slope surface following the primary flow reversal (Videos 2–4). The flow front is maintained for the remainder of the experiment following

repeated episodes of secondary flow reversal on the slope surface and the re-establishment of the parental flow (Videos 2–4). The height upslope at which the flow front develops, the velocity structure, and the frequency of secondary flow reversals recorded on the slope surface and at the base of slope, is a function of slope angle.

At 20°, a flow front with a linear trace, forms at an average height of 0.11 m upslope, one times the flow height, across the width of the slope (Video 2; Fig. 11A). However, the height of the flow front fluctuates between 0.10 and 0.14 m upslope as the flow repeatedly reverses downslope before the flow re-establishes (Video 2). The streamwise velocity fluctuates between 0.02 and -0.02 m s^{-1} , and the cross-stream velocity between 0.01 and -0.01 m s^{-1} (Fig. 8A and B). At 30°, the flow front develops approximately 0.10 m upslope, 0.91 times the flow height, with a weakly sinusoidal trace (Video 3; Fig. 11B). At 30°, the streamwise

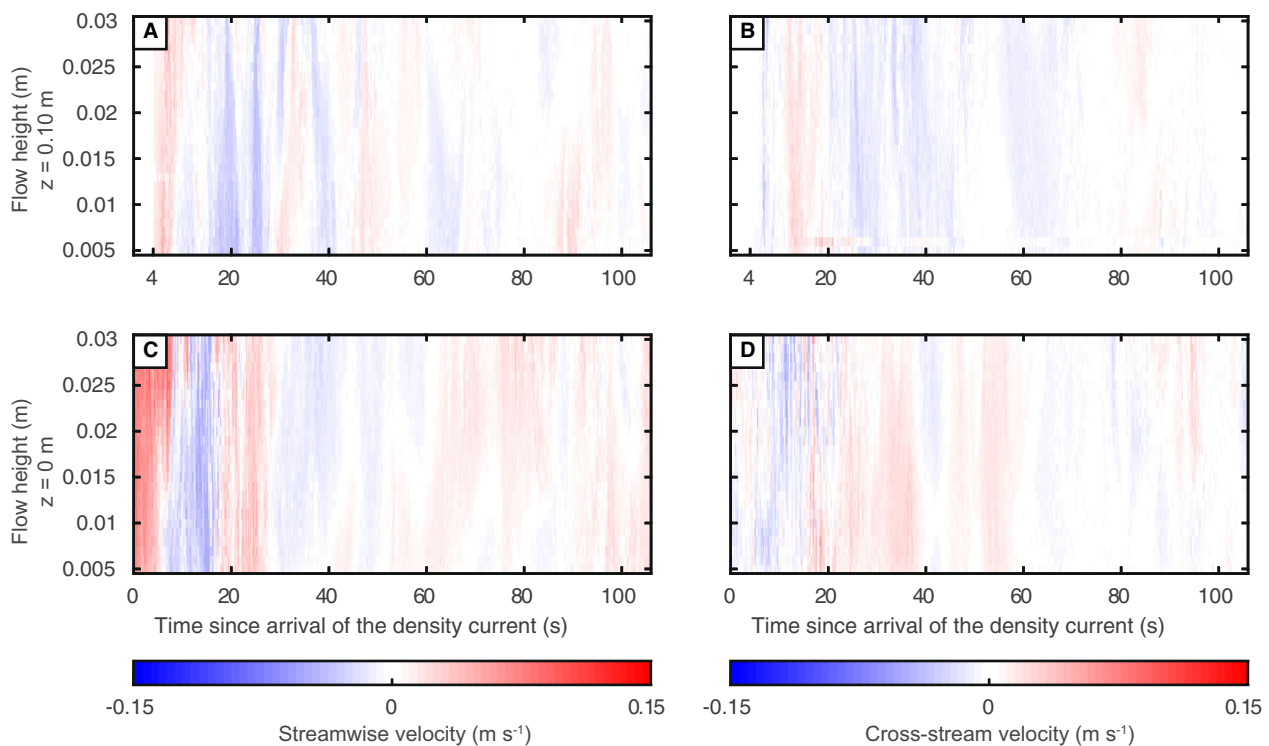


Fig. 9. Acoustic Doppler velocity profiler (ADV) velocity time series of saline density currents interacting with the 30° slope. (A) and (B) Streamwise and cross-stream velocity time series respectively ($z = 0.10$ m upslope). (C) and (D) Streamwise and cross-stream velocity time series respectively ($z = 0$ m, base of slope). The clipped data from the first 4 s in (A) and (B) represents the time taken for the flow to travel from the base of slope to 0.1 m upslope.

velocity of the flow front fluctuates between 0.01 and -0.01 m s^{-1} (Fig. 9A), and the episodes of secondary flow reversal and re-establishment are less defined compared to the 20° slope (Fig. 8A). At 40°, the initial development of the flow front coincides with greatest cross-stream velocity fluctuations (approximately 0.05 m s^{-1}) of any slope configuration (Fig. 10B). For approximately 40 s following the establishment of the flow front, the cross-stream velocity signal is maintained at approximately 0.05 m s^{-1} , whereas the streamwise velocity signal is negligible (Fig. 10A and B). As the positive streamwise velocity at the flow front re-establishes after approximately 50 s (Fig. 10A), the cross-stream velocity becomes negative (approximately -0.02 m s^{-1}) (Fig. 10B). At 40°, the flow front develops approximately 0.13 m upslope, 1.19 times the flow height (Video 4; Fig. 11C).

Single-sided amplitude spectral analysis using a Fast Fourier Transform of the velocity

fluctuations (cf. Dorrell *et al.*, 2018b), at the lowermost ADV measurement point (0.005 m above the base of the tank/slope), was used to assess the frequency of secondary flow reversals (Fig. 12). The lowermost ADV measurement point was used for these analyses as this is closest to the floor, and thus most representative of the conditions affecting sediment transport and deposition. Following the development of the flow front on the slope surface at the 20° and 40° slope (>40 s into flow), low frequency oscillations in the range of approximately 10^0 to 10^{-1} Hz are observed at the middle ADV position (Fig. 12D and P, respectively). The increased power of the oscillations compared to the 30° slope (Fig. 12J) is due to the greater observed fluctuations in the streamwise velocity component (Figs 8A, 9A and 10A). At 20° and 40° the power spectra decrease with height upslope (Fig. 12B, H and N) and dissipate at the base of slope (Fig. 12F, L and R); whereas, at

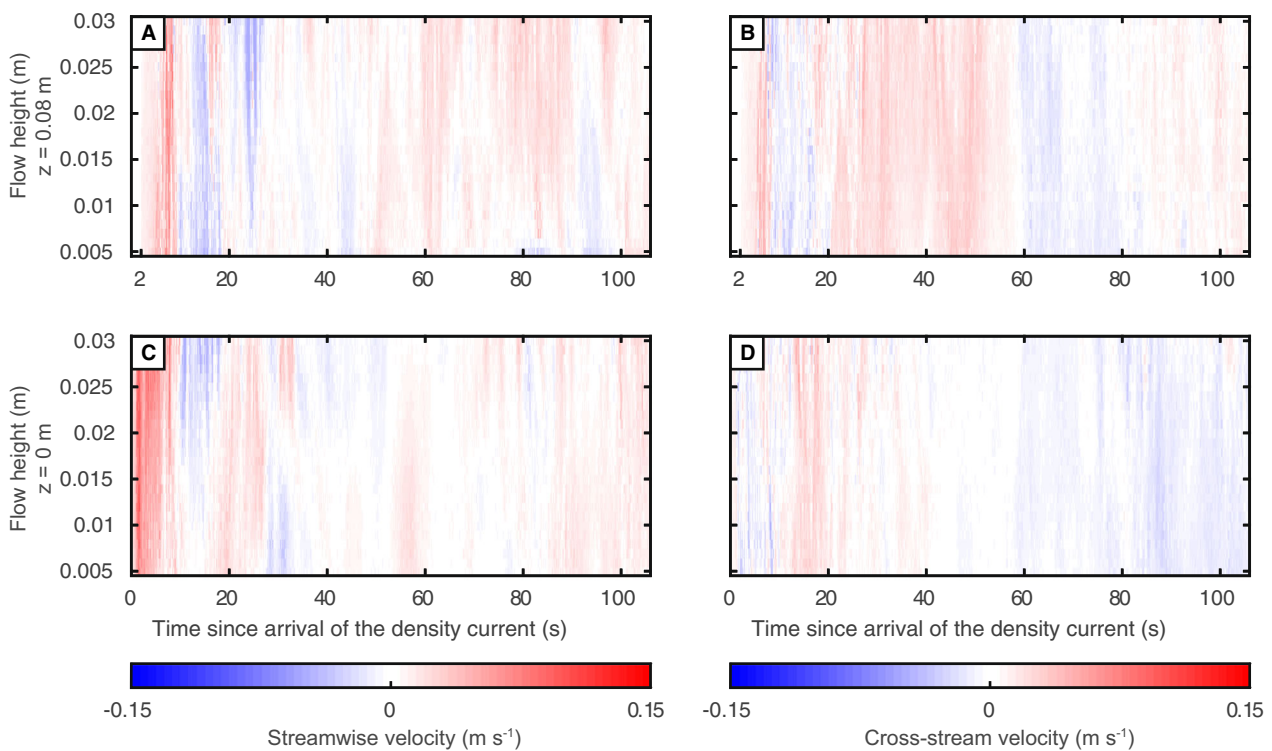


Fig. 10. Acoustic Doppler velocity profiler (ADV) velocity time series of saline density currents interacting with the 40° slope. (A) and (B) Streamwise and cross-stream velocity time series respectively ($z = 0.08$ m upslope). (C) and (D) Streamwise and cross-stream velocity time series respectively ($z = 0$ m, base of slope). The clipped data from the first 2 s in (A) and (B) represents the time taken for the flow to travel from the base of slope to 0.08 m upslope.

30°, the power spectra increase between the middle ADV position (Fig. 12J) and the base of slope (Fig. 12L).

Temporal velocity variability

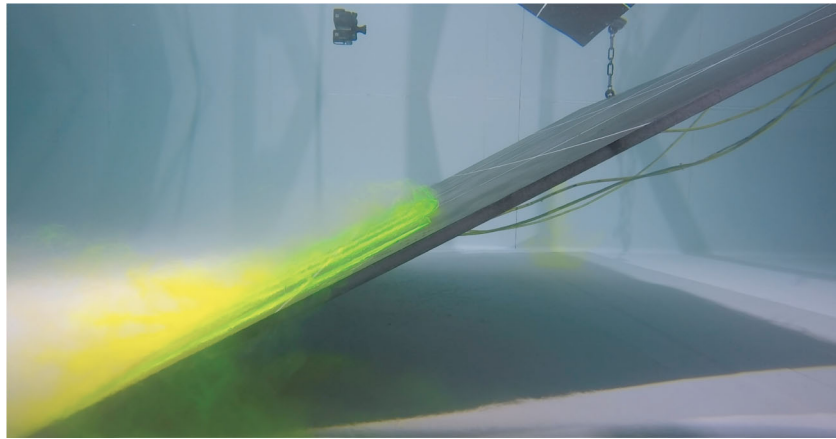
Flow visualization shows the development of complex, multidirectional flows qualitatively, on the slope surface and at the base of slope (Videos 2–4). To better understand the generation of complex, multidirectional flows (i.e. combined flows), the nature of temporal streamwise and cross-stream velocity variations with position (height) on the slope are considered. Here, analysis focusses on the lowermost ADV measurement point (0.005 m above the base of the tank/slope), as measured on the axis of the flow. The incoming flow recorded at the base of each slope (<15 s into flow) has a similar streamwise and cross-stream velocity signal (Fig. 13G to I). The streamwise and cross-stream velocity magnitude and variability decrease through time and with height upslope, in

all cases (Fig. 13). The interaction between the primary flow and the parental flow marks the onset of increased cross-stream velocity variations at the base of the 20° and 30° slopes (Fig. 13G and H). At the base of the 40° slope (Fig. 13I), the streamwise velocity of the primary flow reversal and the cross-stream velocity variability before the establishment of the flow front (<40 s into flow) is decreased compared to the lower slope angle configurations. Whereas, on the slope surface, the ADV data from the 40° slope (Fig. 13F) demonstrate increased streamwise and cross-stream velocity variability compared with the lower slope angle configurations (Fig. 13D and E).

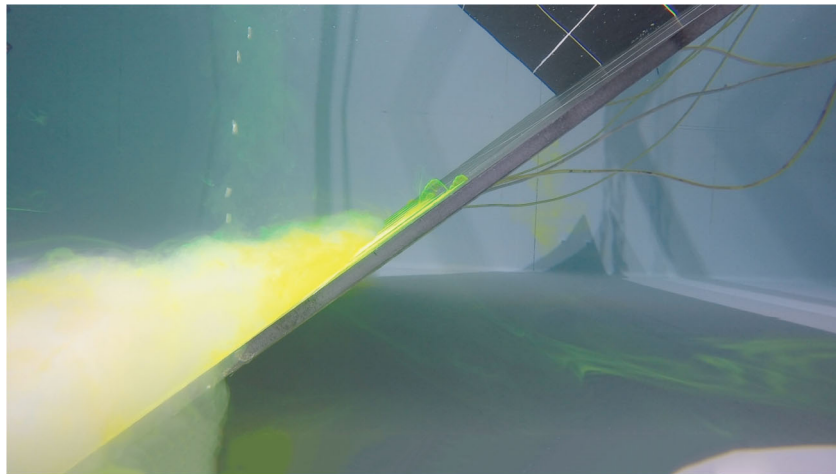
Summary of flow processes

On the slope surface

The increasing slope angle affects the velocity evolution of the density currents (Figs 8, 9 and 10) and the dominant flow processes that operate on the



Video 3: Annotated real-time video illustrating the temporal evolution of the flow with a 30° slope. Fluorescent dye injected at a series of lateral points onto the slope surface was used to visualize the interaction of the density current and the containing topography. Gridded white lines were marked on the slope surface to aid the identification of the height at which the stable flow front developed and the maximum run-up height (h_{\max}).



Video 4: Annotated real-time video illustrating the temporal evolution of the flow with a 40° slope. Fluorescent dye injected at a series of lateral points onto the slope surface was used to visualize the interaction of the density current and the containing topography. Gridded white lines were marked on the slope surface to aid the identification of the height at which the stable flow front developed and the maximum run-up height (h_{\max}).

slope surface (Fig. 14). At 20°, the parental flow is observed to decelerate upslope, with the denser, basal region of the flow becoming weakly reflective as it reverses downslope (Video 2). The upper, dilute region of the flow decouples (or is ‘stripped’) at the density interface and continues upslope whilst rapidly thinning (Fig. 6C and D), with a high degree of lateral flow spreading before reaching h_{\max} (Video 2; Fig. 7A). In the zone of flow stripping on the slope surface, the thin, dilute flow

(Fig. 6D) is observed to diverge away from its axial streamline (Video 2), generating a complex, multi-directional flow (Fig. 13D). The diverging flow reverses downslope, and interacts with the parental flow to generate combined flows high on the slope surface (Video 2; Figs 13D and 14A). At 30°, a change in the dominant flow process compared to the 20° slope (Video 2; Fig. 8C) is supported by: (i) the decreased rate of lateral flow spreading and flow thinning observed on the slope surface

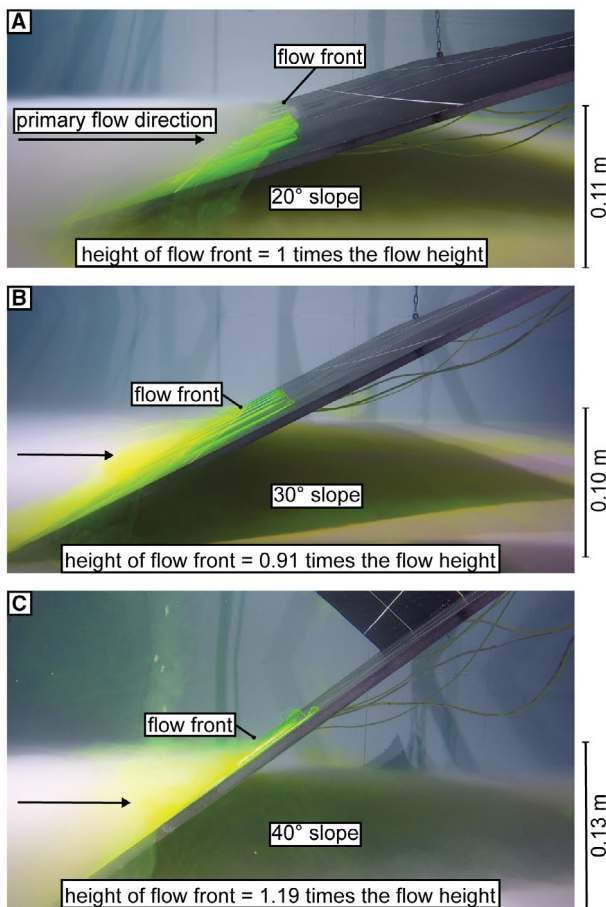


Fig. 11. Photographs captured using an underwater camera, with the height (annotated) at which a quasi-stable flow front develops. (A) 20° slope. (B) 30° slope. (C) 40° slope. At each topographic configuration, a quasi-stable flow front develops on the slope surface following the primary flow reversal of the flow downslope and the subsequent re-establishment of the parental flow.

(Video 3); and (ii) the increased magnitude of the primary flow reversal recorded by the earlier arrival time and increased negative streamwise velocity of the primary flow reversal at the base of slope (Fig. 9C). The increased degree of containment acts to enhance the rate of deceleration at the base of slope (Fig. 9C) and limit the upslope-momentum of the incoming flow (Video 3). As a result, the flow becomes strongly reflective (Fig. 14B). At 40°, the observed decrease in h_{\max} and the degree of flow thinning on the slope surface (Video 4) indicate that the increased topographic containment dramatically decreases the upslope-momentum of the incoming flow. Following the arrival of the flow at the base of slope, part

of the flow is observed to flow approximately normal to the orientation of the slope (Video 4; Fig. 10C). The limited upslope-momentum and flow deflection at the base of slope has the effect of reducing the magnitude of the primary flow reversal at the base of slope (Fig. 10C) compared with the 20° and 30° slopes (Figs 8C and 9C, respectively), and increasing the cross-stream velocity of the flow both on the slope surface and at the base of slope (Fig. 14C, F and I). The superimposition of the strongly deflective flow with the parental flow generates highly multidirectional flows (i.e. combined flows) both at the base of, and low down on, the slope surface (Fig. 13I and F).

At the base of slope

In all topographic configurations, highly multidirectional flows are generated at the base of each flow, both at the base of, and on, the slope (Fig. 13D to I), and flow inflation occurs at the base of slope (Videos 2–4). These changes in flow behaviour result from the interaction of the primary flow reversal with the parental flow (Videos 2–4). The decreased magnitude of the primary flow reversal and degree of flow inflation recorded at the base of the 20° and 40° topographic configurations is attributed to the high-degree of lateral flow spreading at 20° (Fig. 8C), and the reduced upslope-momentum of the flow at 40° (Fig. 10C). Flow divergence and flow deflection are the primary flow process at 20° and 40°, respectively (Fig. 14A and C). At 30°, the magnitude of the first flow reversal recorded at the base of slope is greater than the other slope configurations (Fig. 9C), which is attributed to flow reflection being the dominant flow process (Fig. 14B) and an enhanced interaction between the reflected flow and the parental flow at the base of slope (Video 3). The observed episodes of secondary flow reversal and flow stasis (Figs 8C, 9C and 10C) indicate the quasi-steady state of the density current as it inflates at the base of slope, before subsequently dissipating farther into the experimental basin, upstream of the topographic slope (Videos 2–4).

DISCUSSION

Effect of topographic containment on flow processes

On the slope surface

Here, the incidence of unconfined, 3D density currents upon planar frontal topographic slopes

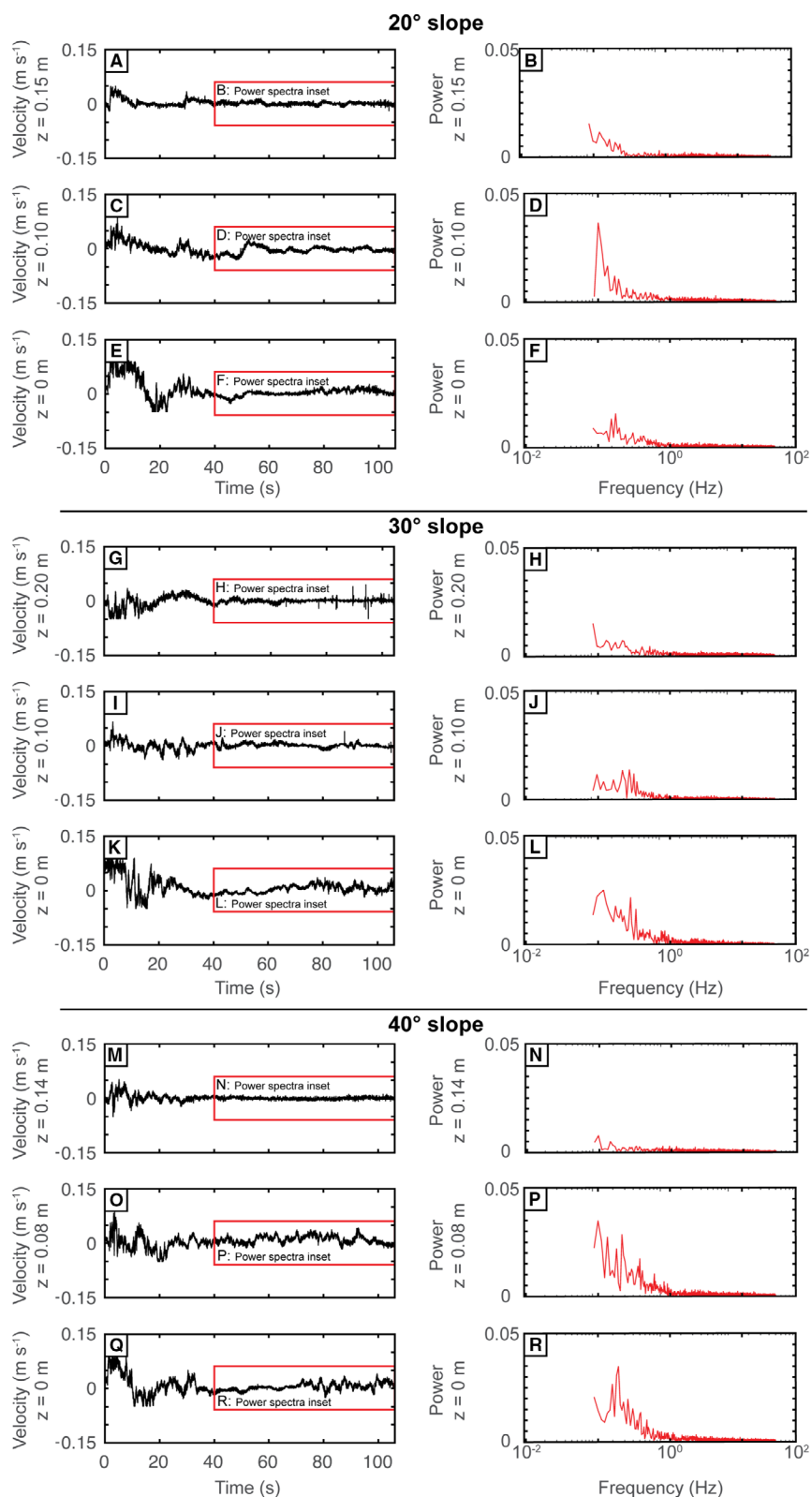


Fig. 12. Acoustic Doppler velocity profiler (ADV) streamwise velocity time series and associated single-sided amplitude spectrum of the streamwise velocity fluctuations from each slope configuration and ADV position. The lowermost ADV data point was used (0.005 m above the base of the tank/slope surface), as this is the most representative of the conditions affecting sediment transport and deposition. (A), (C) and (E) 20° slope, (H), (J) and (L) 30° slope, and (N), (P) and (R) 40° slope, streamwise velocity time series. z = height of the ADV upslope. The inset boxes display the region used in calculating the single sided amplitude spectrum of the streamwise velocity fluctuations, (B), (D) and, (F) 20° slope, (I), (K) and (M) 30° slope, and (O), (Q) and (S) 40° slope.

is shown to result in differences in the superlevation, the degree of flow thinning, and the velocity structure of the flow between the three slope angle configurations. In previous 2D experimental studies (e.g. Pantin & Leeder, 1987; Kneller *et al.*, 1991, 1997; Edwards *et al.*, 1994; Patacci *et al.*, 2015) where flows were strongly confined by the experimental basin, flow reflection has been documented as the dominant flow process with both orthogonal (e.g. Pantin & Leeder, 1987; Edwards *et al.*, 1994; Kneller *et al.*, 1997; Patacci *et al.*, 2015) and oblique (e.g. Kneller *et al.*, 1991) slopes. The inability of the density currents to radially-expand in 2D experiments poorly models the behaviour of natural turbidity currents in unconfined and weakly confined settings. Where unconfined gravity currents have been documented to interact with orthogonal counter-slopes, both in physical (e.g. Soutter *et al.*, 2021) and numerical (e.g. Howlett *et al.*, 2019) models, the decreased containment factor compared to the current study permits the flows to surmount the topography and bypass down-dip. The model presented here shows how the flow process regime changes from divergence-dominated, through reflection-dominated, to deflection-dominated as the slope angle increases from 20° to 30° to 40°, respectively. The new model has implications for the generation of combined flows and potentially for facies and bedforms on topographic slopes.

At the base of slope

The experiments show how a sustained flow input in an unconfined experimental setting results in the inflated density current dissipating throughout the basin, upstream of the topographic slope and/or being diverted around the basal edges of the slope, and the absence of flow ponding. By contrast, in experimental mini-basin settings, sustained flow input results in the progressive infilling of sediment in the first basin (up-dip of the topographic sill), until complete flow ponding results in overspill into the second basin (Brunt *et al.*, 2004). The conditions

for flow ponding, and the development of a marked density boundary in the suspension, are further promoted in 2D flume tank experiments due to the high degree of flow confinement and topographic containment (e.g. Lamb *et al.*, 2004; Patacci *et al.*, 2015). Internal waves have been described as forming at a prominent density boundary in ponded suspensions (Patacci *et al.*, 2015).

Absence of internal waves in unconfined density currents

The lack of distinct peaks in the frequency spectra generated at the mid-slope and base of slope positions (Fig. 12), and the observed absence of well-defined internal wave-like structures (Videos 2–4), suggests that features including solitons and bores are not present in these unconfined density current experiments. Instead, these experiments demonstrate the generation of combined flows both on the slope surface and at the base of slope. Combined flows are generated due to the interaction of unconfined density currents with topographic slopes, and the superimposition of multidirectional flow components (Fig. 13), following flow thinning, deceleration and reversal on the slope surface (Videos 2–4). Solitons and internal bores recognized in 2D experiments have been linked to the generation of an oscillatory flow component and the inception of combined flow (e.g. Pantin & Leeder, 1987; Edwards *et al.*, 1994; Kneller *et al.*, 1997). These observations have been invoked to explain the presence of combined flow bedforms, such as hummock-like structures and symmetrical megaripples above topographic slopes in deep-water settings following flow interactions with seafloor topography (e.g. Privat *et al.*, 2021, 2024; Tinterri *et al.*, 2022; Martínez-Doñate *et al.*, 2023; Siwek *et al.*, 2023). A new model for the generation of combined flow in unconfined density currents has implications for interpreting the degree of flow confinement and topographic containment in deep-water systems.

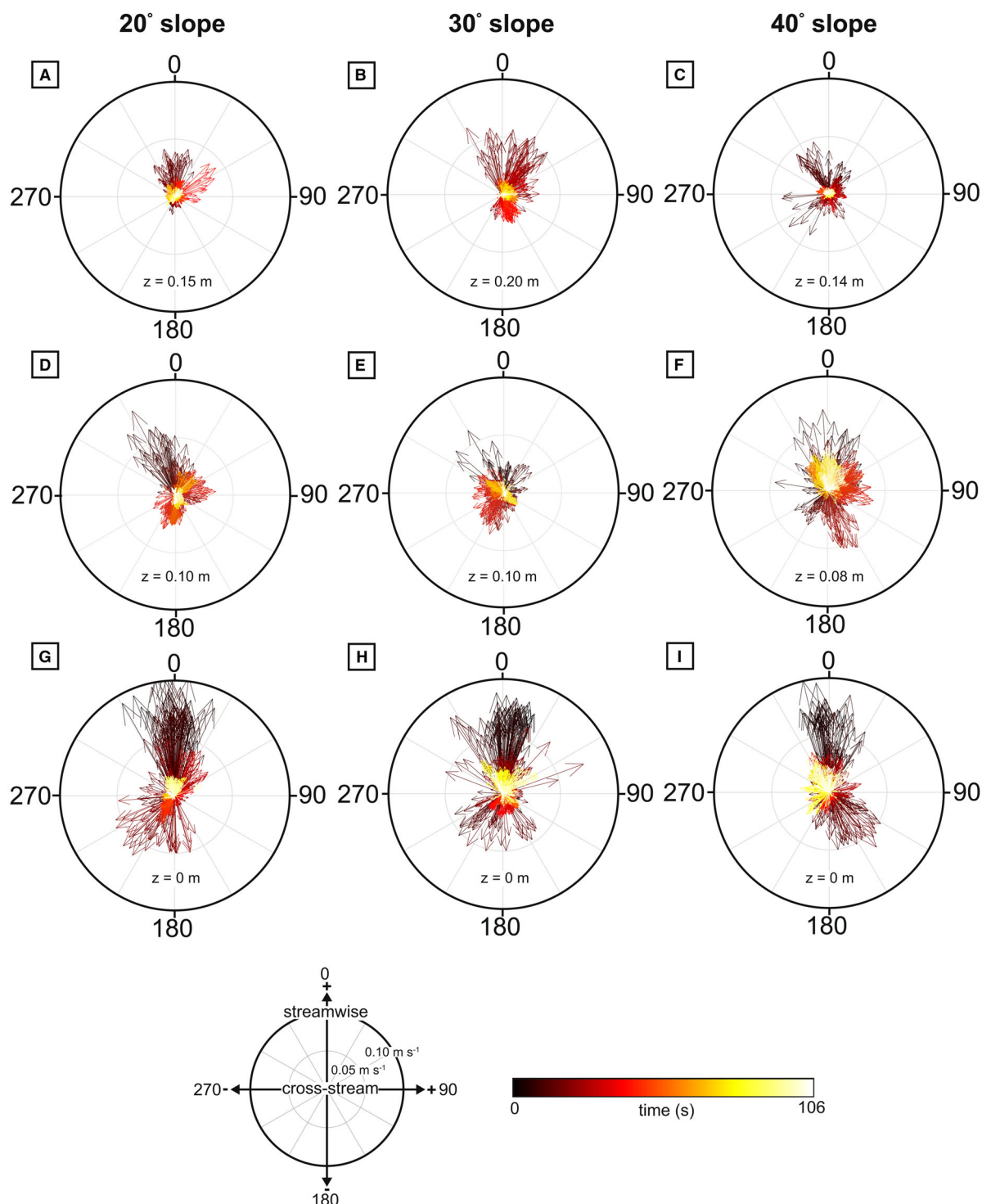


Fig. 13. Streamwise and cross-stream velocity vector variability for the duration of the experimental runs. (A), (B) and (C) at the uppermost ADV position on the slope surface, (20°, 30° and 40° respectively), (D), (E) and (F) at the middle ADV position (20°, 30° and 40° respectively), (G), (H) and (I) at the base of each slope configuration (20°, 30° and 40° respectively). z = height of the ADV upslope. For each experimental run, the 100 Hz ADV data were decimated to 10 Hz, and the lowermost ADV data point was used (0.005 m above the base of the tank/slope surface), as this is most representative of the conditions affecting sediment transport and deposition. The colour gradient represents time (s) in the experiments.

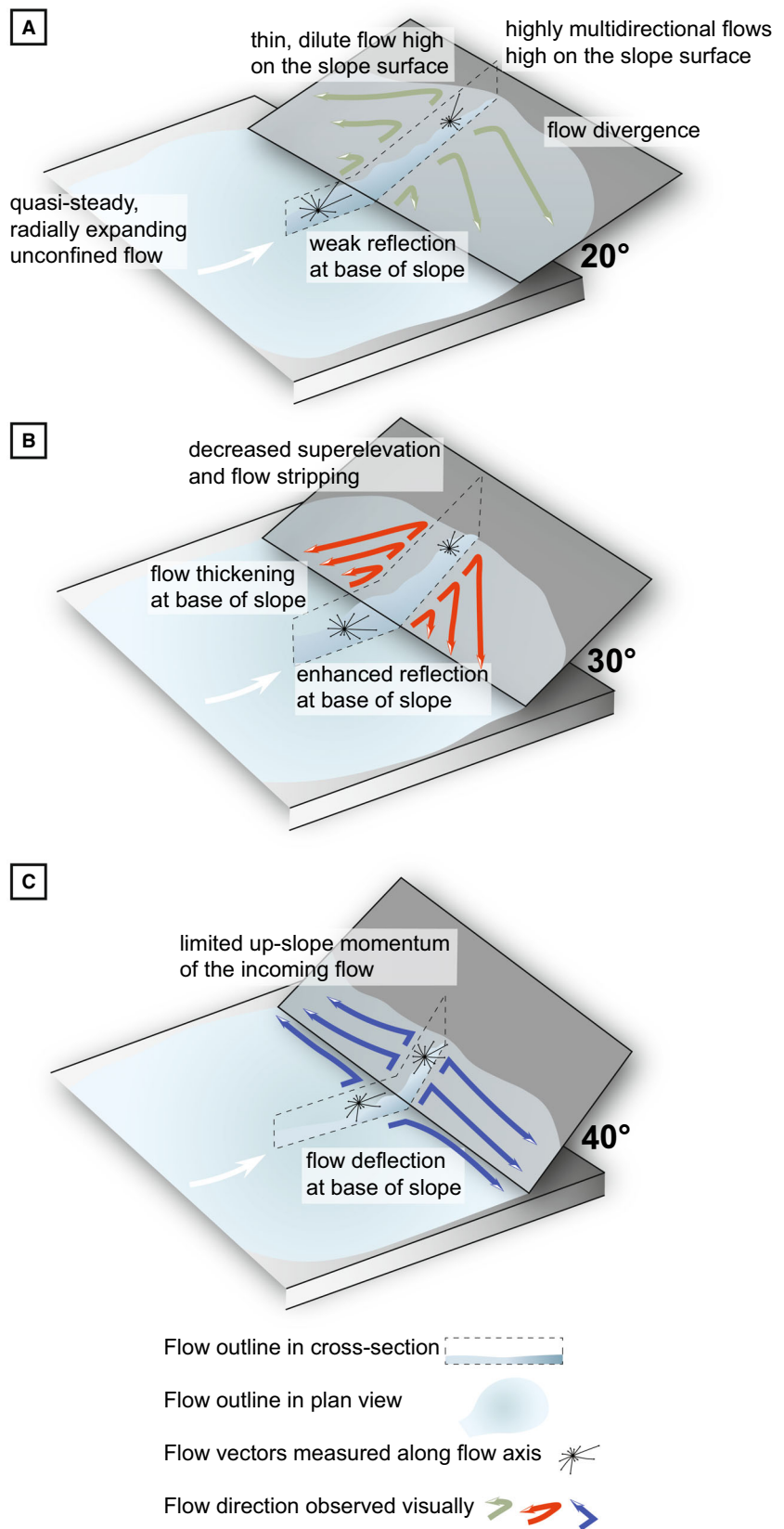


Fig. 14. Schematic three-dimensional summary of the primary flow processes active upon the incidence of the unconfined density current, as a function of the three slope configurations. (A) 20° slope – flow divergence is active in the enhanced zone of flow stripping that forms on the slope surface. (B) 30° slope – flow reflection is the dominant process and produces a flow reversal with an increased magnitude and enhanced flow thickening at the base of slope. (C) 40° slope – flow deflection at the base of slope limits run-up potential and generates a weakly collapsing flow.

A new model for combined flow generation

Here, the generation of combined flows from physical 3D experiments of density currents is explored. At 20°, compared to the 30° and 40° slope configurations, the increased degree of flow stripping, lateral flow spreading and h_{\max} (Video 2), is observed to generate thin, dilute currents high on the slope surface (Fig. 6D). In this position, the diminished gravitational forces that would otherwise act to ‘pull’ the flow back down the slope allows for the dilute flow to spread laterally and strongly diverge away from the axial centreline (Video 2). The superimposition of the multi-directional, diverging flow as it begins to reverse downslope with the unidirectional, yet radially-expanding, parental flow, produces velocity signals with a high-degree of spatio-temporal, streamwise and cross-stream velocity variability on the slope surface (Fig. 13D) and at the base of slope (Fig. 13G). At 30°, the generation of complex, multi-directional flows is focussed towards the base of slope (Fig. 13H). The increased topographic containment leads to flow reflection and the enhanced interaction between the primary flow reversal and the parental flow (Video 3). At 40°, the enhanced flow deflection at the base of slope, due to the increased degree of containment, produces complex, multidirectional flows with a strong cross-stream component, both at the base of slope (Fig. 13I) and low on the slope surface (Fig. 13F). Critically, the results herein document how flow reflection is not the dominant flow process in 3D, unconfined experiments on low angle slopes, unlike in previous 2D experiments (e.g. Pantin & Leeder, 1987; Edwards *et al.*, 1994; Kneller *et al.*, 1997). This highlights that the superelevation of gravity currents, flow divergence and the generation of highly multidirectional flows (i.e. combined flows) is likely to be further enhanced on lower angle slopes, less than 20°, with implications for bedform distribution and onlap styles discussed herein. For each topographic configuration, there is an absence of internal waves (Videos 2–4; Fig. 12). This variability in velocity and direction suggests that the generation of combined flows at different positions at the base of, and on, the slope is a function of the degree of topographic containment.

In deep-marine settings, one mechanism invoked for the generation of combined flows is the superimposition of high-frequency flow oscillations over periods of hours and/or days, against a unidirectional turbidity current (e.g.

Tinterri, 2011). These oscillations are postulated to be generated by the interaction of turbidity currents with seafloor topography, leading to the formation of internal waves. Previous field-based outcrop models (e.g. Tinterri *et al.*, 2016, 2022; Privat *et al.*, 2021, 2024; Martínez-Doñate *et al.*, 2023) have invoked this model to interpret sedimentary structures. However, the model is based largely on semi-quantitative (Edwards *et al.*, 1994) and quantitative (Kneller *et al.*, 1997) observations from 2D, non-ponded flume tank experiments.

A second mechanistic model for combined flow generation exists for ponded turbidity currents, whereby the formation of internal waves is independent of flow interactions with a containing slope (e.g. Patacci *et al.*, 2015). The intensity of the internal waves was attenuated with depth (Patacci *et al.*, 2015), seemingly exerting no direct influence on the bedload. The observations from the Patacci *et al.* (2015) model suggest that internal wave generation is: (i) promoted in 2D, ponded experimental settings, due to the strong stratification focussed at the internal velocity, and concentration and grain-size interface; (ii) dependent on the flow magnitude in 2D experimental settings; and (iii) not applicable to combined flow generation in 3D density current experiments. Internal wave formation in ponded suspensions is hypothesized to exploit the contrast between the velocity, and the concentration and grain-size layers (e.g. Patacci *et al.*, 2015). From experimental modelling of 2D gravity currents, internal wave formation has also been observed to occur at a critical layer within the body of gravity currents, at the height of the maximum internal velocity, thus suggesting that the ‘steady’ body of gravity currents has inherent instabilities in the form of internal waves, and may not be as steady as first assumed (e.g. Marshall *et al.*, 2021, 2023). Internal wave generation has been documented to enhance flow stratification, by maintaining the momentum in the lower-part of the flow and limiting the entrainment of ambient water in the upper-part (Dorrell *et al.*, 2019). The experiments herein model low-density gravity currents with the absence of a strong density stratification. It is hypothesized that gravity currents with a stronger density stratification may have a propensity to develop internal waves and reflected bores, as has been observed in the previous 2D experiments with increased flow densities compared to the current study (e.g. Kneller *et al.*, 1991; Edwards *et al.*, 1994; Kneller, 1995; Patacci *et al.*, 2015). The effects of flow stratification regarding the

implications for the formation of sedimentary structures and different onlap styles is considered in the *Effects of flow stratification* Discussion section. Whether the same mechanisms for internal wave generation are applicable in 3D, unconfined settings with low-density gravity currents is yet to be explored.

Based on the observations from these experiments, a new model is proposed for the generation of combined flows at the base of density currents that interact with simple containing topographies. Combined flows are established following flow deceleration, thinning and spreading on the slope surface, and the superimposition of the reversing flow with the parental flow at the base of slope. Hence, combined flows in unconfined flows are generated in the absence of internal waves. The temporal nature of the complex, multidirectional flows (i.e. combined flows) varies markedly in 3D space depending on the slope angle. Furthermore, the interaction of flows with non-planar seafloor relief, rugose flow fronts and unsteady flows, likely further enhance the generation of combined flows above slopes.

Implications for facies variations

A new model for the formation of hummocks in the deep sea

Hummock-like structures have been documented in a range of deep-marine settings, including basin-plain lobes (e.g. Mulder *et al.*, 2009; Bell *et al.*, 2018), channel-lobe transition zones (e.g. Hofstra *et al.*, 2018) and intraslope lobes (e.g. Privat *et al.*, 2021, 2024; Martínez-Doñate *et al.*, 2023). They are dominantly aggradational and differ in their internal architecture compared to both true HCS, and to supercritical bedforms such as antidunes (see reviews in Tinterri, 2011, and Hofstra *et al.*, 2018); thus they are considered to be the product of subcritical flows. Prave & Duke (1990) and Mulder *et al.* (2009) invoke standing to weakly migrating waves formed by Kelvin–Helmholtz instabilities at the upper flow interface to explain the development of HCS-like bedforms. However, the primary model ascribed to their genesis is based on observations of bores in 2D reflected density current experiments (e.g. Edwards *et al.*, 1994) and applied to outcrop models in confined/contained-reflected basins (e.g. Tinterri, 2011; Tinterri *et al.*, 2016).

The documentation of combined flow in unconfined, subcritical, density currents that interact with planar topography, which form in the absence of oscillatory flow from internal and

surface waves, allows a new mechanistic model for the deposition of hummock-like structures to be proposed. Hummock-like bedforms in these settings are proposed to form via rapid sediment fallout as flows decelerate on the slope, under combined flows that show marked temporal variations in flow directions (Fig. 13). High-up on low angle slopes where the range of flow directions is diverse, and the primary current velocity is low, the hummock-like structures will be composed of convex or concave draping laminae that may largely lack cross-cutting relationships (Figs 15A and 16C), as observed in examples in outcrop and core (Privat *et al.*, 2021, 2024; Taylor *et al.*, 2024). In part, these are analogous to isotropic hummocky cross-stratification, although the absence of cross-cutting relationships is in marked contrast to true HCS (Harms, 1969). Further down the slope where the primary flow is greater and reversals more important, cross-cutting relationships are likely to be more frequent (e.g. Hofstra *et al.*, 2018), producing bedforms in part analogous to anisotropic HCS (Figs 15C and 16C). In all cases, however, higher frequency wave oscillations are not a factor in the generation of the hummocks.

Spatial distribution of bedforms on the slope

As particulate currents decelerate upon incidence with seafloor topography, suspended sediment fallout rates increase, the unidirectional component of the flow decreases, and the flows become strongly multi-directional high up on the slope surface (Fig. 16A and B). More isotropic hummock-like structures are predicted to form under such combined flows high up on low angle slopes (Figs 15A, 16B and 16C), including slopes lower than 20°, where enhanced superelevation and flow divergence are hypothesized to occur. In contrast, the superimposition of the primary flow reversal with the unidirectional flow at the base of each slope configuration is predicted to lead to the deposition of 2D, anisotropic hummock-like structures perpendicular to the slope (Fig. 15C). At 40°, the flow lines of the depletive density currents are observed to converge at the base of slope (accumulative flow), before running parallel to the slope surface (uniform flow) (see Knelner & McCaffrey, 1999) (Video 4), resulting in a quasi-uniform flow component being generated at the base of the simple orthogonal, steep slope. Towards the base of slope, the superimposition of the uniform flow component running parallel to the slope surface and the depletive, parental

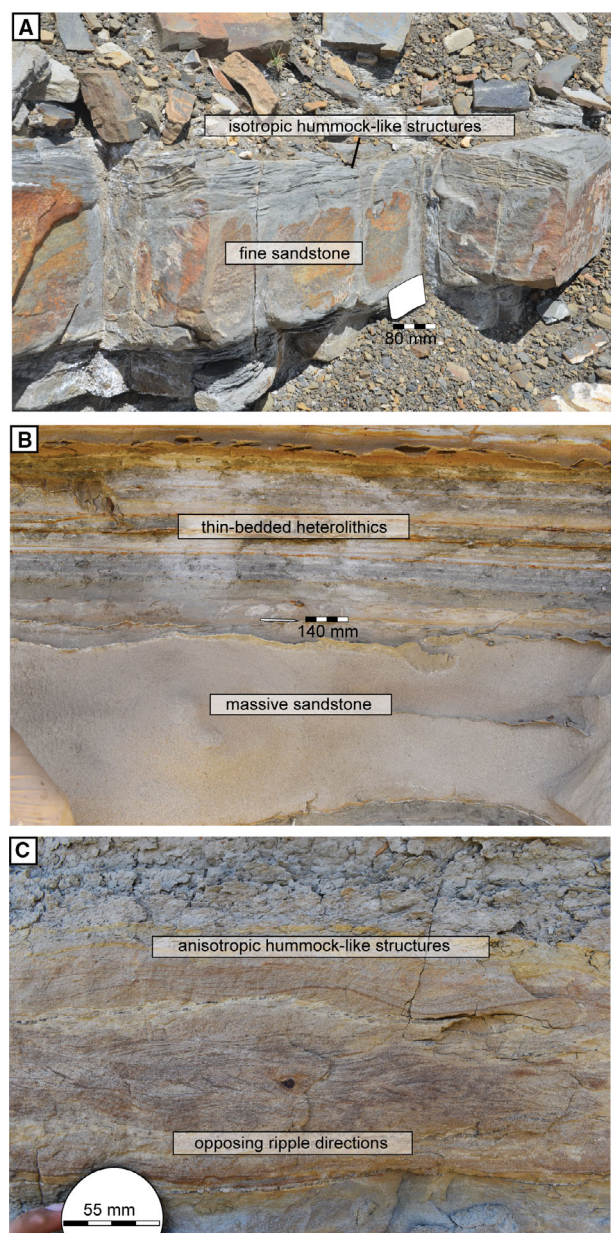


Fig. 15. Facies photographs of turbidites deposited following the interaction with containing topography. (A) Isotropic hummock-like structures displayed in bed-tops (Neuquén Basin, Argentina). (B) Thick, massive sandstone bed (Canyon San Fernando, Baja California, Mexico). (C) Fine sandstone bed displaying ripples with opposing palaeoflow directions, overlain by anisotropic hummock-like structures (Canyon San Fernando, Baja California, Mexico).

flow would support the generation of combined flow bedforms with multidirectional palaeoflow directions (Fig. 16B). Where subcritical density currents decelerate, often towards the base of

impinging slopes or basin margins, outcrop (e.g. Tinterri & Muzzi Magalhaes, 2011; Bell *et al.*, 2018; Tinterri *et al.*, 2022) and experimental (e.g. Allen, 1971, 1973, 1975; McGowan *et al.*, 2024) observations of erosional features (for example, flutes and tool marks) can act to record the regional palaeoflow direction of turbidity currents and/or more mud-rich flows (Peakall *et al.*, 2020). As such, the 2D, hummock-like structures are hypothesized to overprint the regional palaeoflow direction at the base of slope. The new model for the generation of combined flows, and the presence of combined flow bedforms in 3D space on seafloor topography, can be used to reconstruct the form and angle of the topography (Fig. 16B and C).

Development of thick massive sands at the base of slope

Compared to lower angle slope configurations (Videos 2 and 3), the observed rapid flow deceleration at the base of the 40° slope, coupled with the limited upslope momentum (Video 4), is hypothesized to result in high rates of suspended sediment fallout and the formation of thick massive sandstone beds (Fig. 15B), which terminate abruptly at the base of slope (e.g. Schofield & Serbeck, 2000; McCaffrey & Kneller, 2001; Lee *et al.*, 2004) (Fig. 16B and C). The presence of thick massive sandstone beds at the base of slope could therefore provide evidence of flow interactions with seafloor topography. The proposed mechanism for massive sand formation at the base of slope can be considered alongside other mechanisms for the deposition of deep-water massive sands (e.g. Kneller & Branney, 1995; Cantero *et al.*, 2012; Hernandez-Moreira *et al.*, 2020).

Draping onlap of low angle slopes

The increased run-up potential of the dilute flow on the 20° slope that decouples from the co-genetic dense lower region (Fig. 6D; Video 2), demonstrates how lower-concentration flows and the more dilute regions of co-genetic flows are able to drape low-angle onlap surfaces (e.g. Bakke *et al.*, 2013) (Fig. 16). Where the slope angle is below 20°, the superelevation of the dilute part of the flow is hypothesized to increase, further draping the onlap surface with fine-grained material high on the slope surface. As the dilute, upper region of the flow thins and decelerates upslope, the denser region has limited upslope momentum, and rapidly decelerates at the base of slope (Video 3). The modelled behaviour of the denser region of the flow would result in the

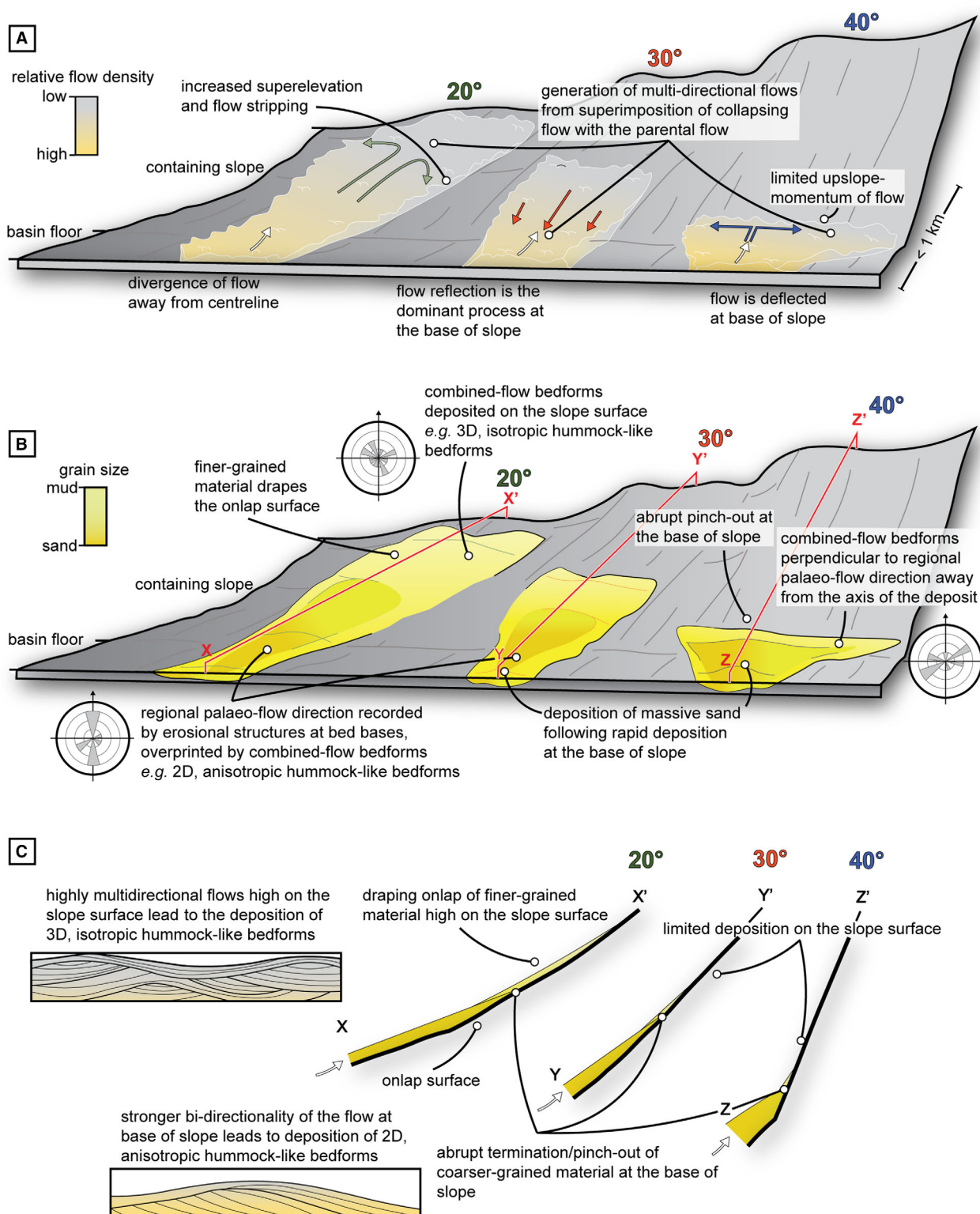


Fig. 16. Summary schematic diagram showing: (A) the dominant flow processes observed from these experiments as a result of low-density gravity currents interacting with topographic slopes of varying angles; (B) the hypothetical deposit geometry for each topographic configuration, and the key facies and palaeo-current dispersal trends; and (C) the onlap styles for each slope configuration and the differences between two-dimensional anisotropic and three-dimensional isotropic hummock-like bedforms (part C modified from Tinterri, 2011).

deposition of the coarser-grained sediment fraction and the abrupt termination lower on the slope, as observed in previous experimental studies (see fig. 13A and B in Soutter *et al.*, 2021). However, the behaviour of the more dilute (i.e. finer-grained) part of the flow on the slope surface was not explored in the previous experimental studies due to the configuration of the topographic slope (e.g. Soutter *et al.*, 2021). Soutter *et al.* (2019) observed in the Annot Basin, France, the abrupt pinch-out of high-density turbidites and the draping onlap of low-density turbidites onto the same onlap surface. The observations from the experiments herein show that, higher on the slope surface, the thin and decelerated flow would generate combined flows and lead to the deposition of the finer-grained sediment fraction (for example, silt – fine sand) and the development of isotropic hummock-like bedforms (Fig. 16B and C). Coupled with the new model for the generation of combined flow, the onlap style of the resulting deposits can support reconstructions of the orientation and gradient of seafloor topography in deep-water settings.

The effects of flow stratification

The present experiments utilized saline flows; however, stratification is a key aspect of sediment gravity flows, particularly those with a sand-grade component, and is more pronounced than in saline flows (Menard & Ludwick, 1951; Gladstone *et al.*, 2004; Amy *et al.*, 2005; Dorrell *et al.*, 2014). The effects of flow stratification will influence the nature of processes as flows interact with topography, albeit that the full influence is difficult to assess *a priori*. Furthermore, density profiles are absent in the few documented unconfined natural sediment gravity flows (e.g. Lintern *et al.*, 2016; Hill & Lintern, 2022). There are three main aspects of the current study to be considered when assessing how flow stratification may affect flow processes. Firstly, it is hypothesized that the effects of density decoupling and increased superelevation of the upper, dilute region of density currents is enhanced when a strongly stratified flow decelerates upon interacting with topography. Thus, increasing stratification is expected to result in dilute flows with a strong multidirectional flow component higher on the slope surface. Second, it is hypothesized that flows with a pronounced stratification have a propensity for internal wave formation and may produce distinctive bedforms up-dip of topography as internal waves propagate upstream. Finally, it is difficult to predict the

patterns of sedimentation and bedform development linked to the interaction between a well-stratified flow at the base of slope with a dilute, and better mixed, less-stratified flow collapsing downslope. These factors suggest the need for future physical experiments and numerical simulations to explore the effects of more strongly stratified flows as they encounter topography, and more direct monitoring efforts in unconfined settings.

CONCLUSIONS

Froude-scaled physical models of three-dimensional, unconfined density currents interacting with a planar orthogonal slope are used to develop a new mechanistic model for the formation of combined flows in turbidity currents. Flow visualization and high-resolution 3D Acoustic Doppler velocity profiler (ADV) data demonstrate how flow divergence, reflection and deflection are observed to be the dominant flow processes active above 20°, 30° and 40° slopes, respectively. The increased 'superelevation' and flow stripping active on the 20° slope promotes flow divergence and generates complex, multidirectional flows high on the slope surface. At 30°, the extent of flow stripping and lateral flow spreading on the slope surface decreases, and flow reflection becomes the dominant flow process, producing an enhanced flow reversal. This generates increased streamwise and cross-stream velocity variations at the base of slope. At 40°, the increased degree of topographic containment limits the upslope momentum of the flow, and instead deflects the flow at the base of slope.

The generation of complex, multidirectional flows (i.e. combined flows) in the experiments herein are formed due to the superimposition of diverging, reflecting and deflecting flow components with the parental flow at the base of, and on, the slope surface. A new model is developed for the generation of combined flow in unconfined flows, which highlights the 3D nature of the flow and the behaviour of the thin, dilute flow on the slope surfaces. This contrasts with previous 2D experimental studies where combined flows are invoked from the interaction of the unidirectional input flow with an oscillatory flow component generated by internal waves following the interaction of turbidity currents with topographic counter-slopes. Observations from previous 2D experimental studies have provided the basis for the existing outcrop models that document

combined flow bedforms in a host of deep-water settings. The new model for combined flow generation from these 3D experiments provides a novel mechanism for the formation and distribution of combined flow bedforms in turbidites, such as isotropic and anisotropic hummock-like bedforms, and the mechanics of draping onlaps versus abrupt pinch-outs. The onlap style of the resulting deposits when coupled with the new model for the generation of combined flow, can support enhanced palaeogeographical reconstructions and assessments of the degree of flow containment within deep-water systems.

ACKNOWLEDGEMENTS

This work has been conducted by EK as part of his PhD project. We thank Chris Stevenson, an anonymous reviewer, and associate editor Kyle Straub for their perceptive comments that helped to improve the manuscript.

CONFLICT OF INTEREST STATEMENT

The authors have no conflict of interest to declare.

DATA AVAILABILITY STATEMENT

The data that support the findings of this study are available from the corresponding author upon reasonable request.

NOMENCLATURE

| | |
|------------|---|
| Fr_d | densimetric Froude number |
| g | acceleration due to gravity (m s^{-2}) |
| g' | reduced gravity |
| h | flow height (m) |
| h_{\max} | maximum run-up height (m) |
| h' | topographic containment factor |
| Re | Reynolds number |
| U | mean depth-averaged velocity (m s^{-1}) |
| U_{\max} | maximum streamwise velocity (m s^{-1}) |
| P_a | density of the ambient water (kg m^{-3}) |
| P_s | mean depth-averaged density of the current (kg m^{-3}) |
| μ | dynamic viscosity |

REFERENCES

- Allen, J.R.L. (1971) Transverse erosional marks of mud and rocks: their physical basis and geological significance. *Sed. Geol.*, **5**, 167–385.
- Allen, J.R.L. (1973) Development of flute-mark assemblages, 1. Evolution of pairs of defects. *Sed. Geol.*, **10**, 157–177.
- Allen, J.R.L. (1975) Development of flute-mark assemblages, 2. Evolution of trios of defects. *Sed. Geol.*, **13**, 1–26.
- Allen, J.R.L. (1991) The Bouma division A and the possible duration of turbidity currents. *J. Sed. Petrol.*, **61**, 291–295.
- Allen, C., Gomis Cartesio, L.E., Hodgson, D.M., Peakall, J. and Milana, J.-P. (2022) Channel incision into a submarine landslide on a Carboniferous basin margin, San Juan, Argentina: evidence for the role of knickpoints. *Depositional Rec.*, **8**, 628–655.
- Amy, L.A., McCaffrey, W.D. and Kneller, B.C. (2004) The influence of a lateral basin-slope on the depositional patterns of natural and experimental turbidity currents. In: *Deep-Water Sedimentation in the Alpine Foreland Basin of SE France: New Perspectives on the Grès d'Annot and Related Systems* (Eds Joseph, P. and Lomas, S.A.), *Geol. Soc. London. Spec. Publ.*, **221**, 311–330. Geological Society, Bath.
- Amy, L.A., Peakall, J. and Talling, P.J. (2005) Density- and viscosity-stratified gravity currents: insights from laboratory experiments and implications for submarine flow deposits. *Sed. Geol.*, **179**, 5–29.
- Armitage, D.A., Roman, B.W., Covault, J.A. and Graham, S.A. (2009) The influence of mass-transport-deposit surface topography on the evolution of turbidite architecture: the Sierra Contreras, Tres Pasos Formation (Cretaceous), Southern Chile. *J. Sed. Res.*, **79**, 287–301.
- Arnott, R.W. and Southard, J.B. (1990) Exploratory flow-duct experiments on combined-flow bed configurations, and some implications for interpreting storm-event stratification. *J. Sed. Res.*, **60**, 211–219.
- Bakke, K., Kane, I.A., Martinsen, O.J., Peterson, S.A., Johansen, T.A., Hustoft, S., Jacobsen, F.H. and Groth, A. (2013) Seismic modelling in the analysis of deep-water sandstone termination styles. *AAPG Bull.*, **97**, 1395–1419.
- Bell, D., Stevenson, C.J., Kane, I.A., Hodgson, D.M. and Poyatos-Moré, M. (2018) Topographic controls on the development of contemporaneous but contrasting basin-floor depositional architectures. *J. Sed. Res.*, **88**, 1166–1189.
- Brunt, R.L., McCaffrey, W.D. and Kneller, B.C. (2004) Experimental modelling of the spatial distribution of grain size developed in a fill-and-spill mini-basin setting. *J. Sed. Res.*, **74**, 438–446.
- Buckee, C., Kneller, B. and Peakall, J. (2001) Turbulence structure in steady, solute-driven gravity currents. In: *Particulate Gravity Currents* (Eds W. McCaffrey, B. Kneller and J. Peakall), *Int. Assoc. Sedimentol. Spec. Pub.*, **31**, 173–187. Blackwell Science Ltd, Oxford.
- Cantero, M., Cantelli, A., Pirmez, C., Balachandar, S., Mohrig, D., Hickson, T., Yeh, T., Naruse, H. and Parker, G. (2012) Emplacement of massive turbidites linked to extinction of turbulence in turbidity currents. *Nat. Geosci.*, **5**, 42–45.
- Cartigny, M.J., Ventra, D., Postma, G. and Van Den Berg, J.H. (2014) Morphodynamics and sedimentary structures of bedforms under supercritical-flow condition: new

- insights from flume experiments. *Sedimentology*, **61**, 712–748.
- Clifton, H.E. (1976) Wave-formed sedimentary structures, a conceptual model. In: *Beach and Nearshore Sedimentation* (Eds Davies, R.A.J. and Etherington, R.L.), *SEPM Spec. Pub.*, **24**, 126–148. SEPM Society for Sedimentary Geology, Tulsa, OK.
- Cullen, T.M., Collier, R.E.L., Gawthorpe, R.L., Hodgson, D.M. and Barrett, B.J. (2019) Axial and transverse deep-water sediment supply to syn-rift fault terraces: insights from the west Xylokaastro fault block, Gulf of Corinth, Greece. *Basin Res.*, **32**, 1115–1149.
- Cumberpatch, Z.A., Kane, I.A., Soutter, E.L., Hodgson, D.M., Jackson, C.A.-L., Kilhams, B.A. and Poprawski, Y. (2021) Interactions between deep-water gravity flows and active salt tectonics. *J. Sed. Res.*, **91**, 34–65.
- Curry, J.R. and Moore, D.G. (1971) Growth of the Bengal deep-sea fan and denudation in the Himalayas. *Geol. Soc. Am. Bull.*, **82**, 563–572.
- Dorrell, R.M., Darby, S.E., Peakall, J., Sumner, E.S., Parsons, D.R. and Wynn, R.B. (2014) The critical role of stratification in submarine channels: implications for channelization and long run-out flows. *J. Geophys. Res. Oceans*, **119**, 2620–2641.
- Dorrell, R.M., Patacci, M. and McCaffrey, W.D. (2018a) Inflation of ponded, particulate laden density currents. *J. Sed. Res.*, **88**, 1276–1282.
- Dorrell, R.M., Peakall, J., Burns, C. and Keevil, G.M. (2018b) A novel mechanism in sinuous seafloor channels: implications for submarine channel evolution. *Geomorphology*, **303**, 1–12.
- Dorrell, R.M., Peakall, J., Darby, S.E., Parsons, D.R., Johnson, J., Sumner, E.J., Wynn, R.B., Özsoy, E. and Tezcan, D. (2019) Self-sharpening induces jet-like structures in seafloor gravity currents. *Nat. Commun.*, **10**, 1381.
- Duke, W.L., Arnott, R.W.C. and Cheer, R.J. (1991) Shelf sandstones and hummocky cross-stratification: new insights on a stormy debate. *Geology*, **19**, 625–628.
- Dumas, S. and Arnott, R.W.C. (2006) Origin of hummocky and swaley cross-stratification – the controlling influence of unidirectional current strength and aggradation rate. *Geology*, **34**, 1073–1076.
- Edwards, D.A., Leeder, M.R., Best, J.L. and Pantin, H.M. (1994) On experimental reflected density currents and the interpretation of certain turbidites. *Sedimentology*, **41**, 437–461.
- Ellison, T.H. and Turner, J.S. (1959) Turbulent entrainment in stratified flows. *J. Fluid Mech.*, **6**, 423–448.
- Emmel, F.J. and Curry, J.R. (1983) The Bengal Submarine Fan, Northeastern Indian Ocean. *Geo-Mar. Lett.*, **3**, 119–124.
- Gladstone, C., Ritchie, L.J., Sparks, S.J. and Woods, A.W. (2004) An experimental investigation of density-stratified inertial gravity currents. *Sedimentology*, **51**, 767–789.
- Graf, W.H. (1971) *Hydraulics of Sediment Transport*. McGraw Hill, New York, NY. 513 pp.
- Groeneweg, R.M., Hodgson, D.M., Pr  lat, A., Luthi, S.M. and Flint, S.S. (2010) Flow–deposit interaction in submarine lobes: insights from outcrop observations and realizations of a process-based numerical model. *J. Sed. Res.*, **80**, 252–267.
- Harms, J.C. (1969) Hydraulic significance of some sand ripples. *GSA Bull.*, **80**, 363–396.
- Harris, P.T., Macmillan-Lawler, M., Rupp, J. and Baker, E.R. (2014) Geomorphology of the oceans. *Mar. Geol.*, **352**, 4–24.
- Haughton, P.D.W. (1994) Deposits of deflected and ponded turbidity currents, Sorbas Basin, Southeast Spain. *J. Sediment. Res.*, **64**, 233–246.
- Haughton, P.D.W. (2000) Evolving turbidite systems on a deforming basin floor, Tabernas, SE Spain. *Sedimentology*, **47**, 497–518.
- Hernandez-Moreira, R., Jafarinik, S., Sanders, S., Kendall, C.G.S.C., Parker, G. and Viparelli, E. (2020) Emplacement of massive deposits by sheet flow. *Sedimentology*, **67**(4), 1951–1972.
- Hill, P.R. and Lintern, D.G. (2022) Turbidity currents on the open slope of the Fraser Delta. *Mar. Geol.*, **445**, 106738.
- Hilton, V. and Pickering, K.T. (1998) *Turbidite Systems of Southeast France*, p. 229. Vallis Press, London.
- Hiscott, R.N. (1994) Loss of capacity, not competence, as the fundamental process governing deposition from turbidity currents. *J. Sed. Res.*, **64**, 209–214.
- Hodgson, D.M. and Haughton, P.D.W. (2004) Impact of syndepositional faulting on gravity current behaviour and deep-water stratigraphy: Tabernas-Sorbas Basin, SE Spain. In: *Confined Turbidite Systems* (Eds Lomas, S.A. and Joseph, P.), *Geol. Soc. London. Spec. Publ.*, **222**, 135–158.
- Hodgson, D.M., Peakall, J. and Maier, K.L. (2022) Submarine channel mouth settings: processes, geomorphology, and deposits. *Front. Earth Sci.*, **10**, 790320.
- Hofstra, M., Peakall, J., Hodgson, D.M. and Stevenson, C.J. (2018) Architecture and morphodynamics of subcritical sediment waves in ancient channel-lobe transition zone. *Sedimentology*, **65**, 2339–2367.
- Howlett, D.M., Ge, Z., Nemec, W., Gawthorpe, R.L., Rotevatn, A. and Jackson, C.A.-L. (2019) Response of unconfined turbidity currents to deep-water fold and thrust belt topography: orthogonal incidence on solitary and segmented folds. *Sedimentology*, **66**, 2425–2454.
- Howlett, D.M., Gawthorpe, R.L., Ge, Z., Rotevatn, A. and Jackson, C.A.-L. (2021) Turbidites, topography and tectonics: Evolution of submarine channel-lobe systems in the salt-influenced Kwanza Basin, offshore Angola. *Basin Res.*, **33**, 1076–1110.
- Joseph, P., Babonneau, N., Bourgeois, A., Cotteret, G., Eschard, R., Garin, B., Granjeon, D., Lerat, O., Ravenee, C., Domes de Souza, O., Guillocheau, F. and Qemener, J.M. (2000) The Annot sandstone outcrops (French Alps): Architecture description as input for quantification and 3D reservoir modeling. In: *Deep-Water Reservoirs of the World* (Eds Weimer, P., Slatt, R.M., Coleman, J., Rosen, N.C., Nelson, H., Bouma, A.H., Styzen, M.J. and Lawrence, D.T.), Vol. **28**, pp. 422–449. SEPM Society for Sedimentary Geology, Tulsa, OK.
- Kane, I.A. and Hodgson, D.M. (2011) Sedimentological criteria to differentiate submarine channel levee subenvironments: exhumed examples from the Rosario Fm. (Upper Cretaceous) of Baja California, Mexico, and the Fort Brown Fm. (Permian), Karoo basin, S. Africa. *Mar. Petrol. Geol.*, **28**, 807–823.
- Keevil, G.M., Peakall, J., Best, J.L. and Amos, K.J. (2006) Flow structure in sinuous submarine channels: velocity and turbulence structure of an experimental submarine channel. *Mar. Geol.*, **229**, 241–257.

- Kneller, B.** (1995) Beyond the turbidite paradigm: physical models for deposition of turbidites and their implications for reservoir prediction. In: *Characterization of Deep Marine Clastic Systems* (Eds Hartley, A.J. and Prosser, D.J.), Vol. **94**, pp. 31–49. Geological Society, Bath, UK.
- Kneller, B.C. and Branney, M.J.** (1995) Sustained high-density turbidity currents and the deposition of thick massive sands. *Sedimentology*, **42**, 607–616.
- Kneller, B. and Buckee, C.** (2000) The structure and fluid mechanics of turbidity currents: a review of some recent studies and their geological implications. *Sedimentology*, **47**, 62–94.
- Kneller, B.C. and McCaffrey, W.D.** (1995) Modelling the effects of salt-induced topography on deposition from turbidity currents. In: *Salt, Sediment and Hydrocarbons* (Eds Travis, C.J., Vendeville, B.C., Harrison, H., Peel, F.J., Hudec, M.R. and Perkins, B.E.), Gulf Coast Society of Economic Paleontologists And Mineralogists Foundation Sixteenth Annual Research Conference 1995, 137–145. SEPM Society for Sedimentary Geology, Tulsa, OK.
- Kneller, B. and McCaffrey, W.** (1999) Depositional effects of flow nonuniformity and stratification within turbidity currents approaching a bounding slope: deflection, reflection, and facies variation. *J. Sed. Res.*, **69**, 980–991.
- Kneller, B., Edwards, D., McCaffrey, W. and Moore, R.** (1991) Oblique reflection of turbidity currents. *Geology*, **14**, 250–252.
- Kneller, B.C., Bennett, S.J. and McCaffrey, W.D.** (1997) Velocity and turbulence structure of density currents and internal solitary waves: potential sediment transport and the formation of wave ripples in deep water. *Sed. Geol.*, **112**, 235–250.
- Komar, P.D.** (1971) Hydraulic jumps in turbidity currents. *Geol. Soc. Am. Bull.*, **82**, 1477–1488.
- Kuenen, P.H. and Migliorini, C.I.** (1950) Turbidity currents as a cause of graded bedding. *J. Geol.*, **58**, 91–127.
- Lamb, M.L., Hickson, T., Marr, J.G., Sheets, B., Paola, C. and Parker, G.** (2004) Surging versus continuous turbidity currents: flow dynamics and deposits in an experimental intraslope basin. *J. Sed. Res.*, **74**, 148–155.
- Lee, S.E., Amy, L.A. and Talling, P.J.** (2004) The character and origin of thick base-of-slope sandstone units of the Peira Cava outlier, SE France. In: *Deep-Water Sedimentation in the Alpine Foreland Basin of SE France: New Perspectives on the Grès d'Annot and Related Systems* (Eds Joseph, P. and Lomas, S.A.), *Geol. Soc. London. Spec. Publ.*, **221**, 331–3347.
- Lintern, D.G., Hill, P.R. and Stacey, C.** (2016) Powerful unconfined turbidity current captured by cabled observatory on the Fraser River delta slope, British Columbia, Canada. *Sedimentology*, **63**, 1041–1064.
- Marshall, C.R., Dorrell, R.M., Keevil, G.M., Peakall, J. and Tobias, S.M.** (2021) Observations of large-scale coherent structures in gravity currents: implications for flow dynamics. *Exp. Fluids*, **62**, 120.
- Marshall, C.R., Dorrell, R.M., Keevil, G.M., Peakall, J. and Tobias, S.M.** (2023) On the role of transverse motion in pseudo-steady gravity currents. *Exp. Fluids*, **64**, 63.
- Martínez-Doñate, A., Privat, A.M.-L., Hodgson, D.M., Jackson, C.A.-L., Kane, I.A., Spychala, Y.T., Duller, R.A., Stevenson, C., Keavney, E., Schwarz, E. and Flint, S.S.** (2021) Substrate entrainment, depositional relief, and sediment capture: impact of a submarine landslide on flow process and sediment supply. *Front. Earth Sci.*, **9**, 757617.
- Martínez-Doñate, A., Kane, I.A., Hodgson, D.M., Privat, A.M.-L., Jackson, C.A.-L., Schwarz, E. and Flint, S.S.** (2023) Stratigraphic change in flow transformation processes recorded in early post-rift deep-marine intraslope lobe complexes. *Sedimentology*, **70**, 1379–1412.
- McCaffrey, W. and Kneller, B.** (2001) Process controls on the development of stratigraphic trap potential on the margins of confined turbidite systems and aids to reservoir evaluation. *AAPG Bull.*, **85**, 971–988.
- McGowan, D., Salian, A., Baas, J.H., Peakall, J. and Best, J.** (2024) On the origin of chevron marks and striated grooves, and their use in predicting mud bed rheology. *Sedimentology*, **71**, 687–708.
- Méjean, S., François, G., Faug, T. and Einav, I.** (2022) X-ray study of fast and slow granular flows with transition jumps in between. *Granul. Matter*, **24**, 26.
- Menard, H.W. and Ludwick, J.C.** (1951) Applications of hydraulics to the study of marine turbidity currents. In: *Turbidity Currents and the Transportation of Coarse Sediments to Deep Water* (Ed Hough, J.L.), *SEPM Spec. Pub.*, **2**, 2–13. SEPM Society for Sedimentary Geology, Tulsa, OK.
- Middleton, G.V. and Hampton, M.A.** (1973) Subaqueous sediment transport and deposition by sediment gravity flows. In: *Marine Sediment Transport and Environment Management* (Eds Stanley, D.J. and Swift, D.J.P.), pp. 197–218. Wiley, New York.
- Muck, M.T. and Underwood, M.B.** (1990) Upslope flow of turbidity currents: A comparison among field observations, theory, and laboratory models. *Geology*, **18**, 54–57.
- Mulder, T., Razin, P. and Fauget, J.-C.** (2009) Hummocky cross-stratification-like structures in deep-sea turbidites: upper Cretaceous Basque basins (Western Pyrenees, France). *Sedimentology*, **56**, 997–1015.
- Pantin, H.M. and Leeder, M.R.** (1987) Reverse flow in turbidity currents: the role of internal solitons. *Sedimentology*, **34**, 1143–1155.
- Patacci, M., Houghton, P.D.W. and McCaffrey, W.D.** (2015) Flow behavior of ponded turbidity currents. *J. Sed. Res.*, **85**, 885–902.
- Peakall, J., Ashworth, P. and Best, J.** (1996) Physical modelling in fluvial geomorphology: principles, applications and unresolved issues. In: *The Scientific Nature of Geomorphology: Proceedings of the 27th Binghamton Symposium, September 27–29, 1996* (Eds Rhoads, B. and Thorn, C.), pp. 221–253. Hoboken, NJ, Wiley and Sons Ltd.
- Peakall, J., Best, J.L., Baas, J., Hodgson, D.M., Clare, M.A., Talling, P.J., Dorrell, R.M. and Lee, D.R.** (2020) An integrated process-based model of flutes and tool marks in deep-water environments: implications for palaeohydraulics, the Bouma sequence, and hybrid event beds. *Sedimentology*, **67**, 1601–1666.
- Pickering, K.T. and Hiscott, R.H.** (1985) Contained (reflected) turbidity currents from the Middle Ordovician Cloridorme Formation, Quebec, Canada: an alternative to the antidune hypothesis. *Sedimentology*, **32**, 373–394.
- Piper, D.J.W. and Normark, W.R.** (1983) Turbidite depositional patterns and flow characteristics, Navy Submarine Fan, California Borderland. *Sedimentology*, **30**, 681–694.
- Prave, A.R. and Duke, W.L.** (1990) Small-scale hummocky-cross stratification in turbidites; a form of antidune stratification? *Sedimentology*, **37**, 531–539.
- Privat, A.M.-L., Hodgson, D.M., Jackson, C.A.-L., Schwarz, E. and Peakall, J.** (2021) Evolution from syn-rift carbonates to early post-rift deep-marine intraslope lobes:

- the role of rift basin physiography on sedimentation patterns. *Sedimentology*, **68**, 2563–2605.
- Privat, A.M.L., Peakall, J., Hodgson, D.M., Schwarz, E., Jackson, C.A.L. and Arnol, J.A.** (2024) Evolving fill-and-spill patterns across linked early post-rift depocentres control lobe characteristics: Los Molles Formation, Argentina. *Sedimentology*, **71**, 1639–1685.
- Puigdefàbregas, C., Gjelberg, J.M. and Vaksdal, M.** (2004) The Grès d'Annot in the Annot syncline: outer basin-margin onlap and associated soft-sediment deformation. In: *Deep-Water Sedimentation in the Alpine Foreland Basin of SE France: New Perspectives on the Grès d'Annot and Related Systems* (Eds Joseph, P. and Lomas, S.A.), *Geol. Soc. London. Spec. Publ.*, **221**, 367–388. Geological Society, Bath.
- Reece, J.K., Dorell, R.M. and Straub, K.M.** (2024) Circulation of hydraulically ponded turbidity currents and the filling of continental slope minibasins. *Nat. Commun.*, **15**, 2075.
- Schofield, K. and Serbeck, J.** (2000) The 'Above Magenta' reservoir at Ursa Field: a process-response model to explain a classic wire-line signature. In: *Deep-Water Reservoirs of the World: Gulf Coast Section Society of Economic Paleontologists and Mineralogists Foundation 20th Annual Bob F. Perkins Research Conference* (Eds Weimer, P., Slatt, R.M., Coleman, J., Rosen, N.C., Nelson, H., Bouma, A.H., Styzen, M.J. and Lawrence, D.T.), pp. 894–910. SEPM Society for Sedimentary Geology, Tulsa, OK.
- Seabrook, S., Mackay, K., Watson, S.J., Clare, M.A., Hunt, J.E., Yeo, I.A., Lane, E.M., Clark, M.R., Wysoczanski, R., Rowden, A.A., Kula, T., Hoffmann, L.J., Armstrong, E. and Williams, M.J.M.** (2023) Volcaniclastic density currents explain widespread and diverse seafloor impacts of the 2022 Hunga Volcano eruption. *Nat. Comm.*, **14**, 7881.
- Simpson, J.E.** (1997) *Gravity Currents in the Environment and Laboratory*, 2nd edn. Cambridge University Press, Cambridge. 244 pp.
- Sinclair, H.D.** (1994) The influence of lateral basin slopes on turbidite sedimentation in the Annot sandstones of SE France. *J. Sediment. Res.*, **64**, 42–54.
- Siwek, P., Waśkowska, A. and Wendorff, M.** (2023) Mud-rich low-density turbidites in structurally-controlled intraslope mini-basin: the influence of flow containment on depositional processes and sedimentation patterns (Szcza, Oligocene, Polish Outer Carpathians). *Sedimentology*, **70**, 1741–1784.
- Smith, R. and Joseph, P.** (2004) Onlap stratal architectures in the Grès d'Annot: geometric models and controlling factors. In: *Deep-Water Sedimentation in the Alpine Basin of SE France: New Perspectives on the Grès d'Annot and Related Systems* (Eds Joseph, P. and Lomas, S.A.), Vol. **221**, pp. 389–399. Geological Society, Bath, UK.
- Soutter, E.L., Kane, I.A., Fuhrmann, A., Cumberpatch, Z.A. and Huuse, M.** (2019) The stratigraphic evolution of onlap in siliciclastic deep-water systems: Autogenic modulation of allogenic signals. *J. Sed. Res.*, **89**, 890–917.
- Soutter, E.L., Bell, D., Cumberpatch, Z.A., Ferguson, R.A., Spychala, Y.T., Kane, I.A. and Eggenhuisen, J.T.** (2021) The influence of confining topography orientation on experimental turbidity currents and geological implications. *Front. Earth Sci.*, **8**, 540633.
- Spychala, Y.T., Hodgson, D.M., Stevenson, C.J. and Flint, S.S.** (2017) Aggradational lobe fringes: The influence of subtle intrabasinal seabed topography on sediment gravity flow processes and lobe stacking patterns. *Sedimentology*, **64**, 582–608.
- Sumner, E.J., Peakall, J., Parsons, D.R., Wynn, R.B., Darby, S.E., Dorrell, R.M., McPhail, S.D., Perrett, J., Webb, A. and White, D.** (2013) First direct measurements of hydraulic jumps in an active submarine density current. *Geophys. Res. Lett.*, **40**, 5904–5908.
- Talling, P.J., Cartigny, M.J.B., Pope, E., Baker, M., Clare, M.A., Heijnen, M., Hage, S., Parson, D.R., Simmons, S.M., Paull, C.K., Gwiazda, R., Lintern, G., Hughes Clarke, J.E., Xu, J., Silva Jacinto, R. and Maier, K.L.** (2023) Detailed monitoring reveals the nature of submarine turbidity currents. *Nat. Rev. Earth. Environ.*, **4**, 642–658.
- Taylor, W.J., Hodgson, D.M., Peakall, J., Kane, I.A., Morris, E.A. and Flint, S.S.** (2024) Unidirectional and combined transitional flow bedforms: controls on process and distribution in submarine slope settings. *Sedimentology*, **71**, 1329–1362.
- Tinterri, R.** (2006) Proposal for a classification scheme for combined flow sedimentary structures and the meaning of sigmoidal- and hummocky-cross stratification in facies analysis. Proceedings Annual Meeting, Italian Sedimentology Group GEOSD, Modena, 26–27 September 2006, 111.
- Tinterri, R.** (2007) The lower Eocene Roda Sandstone (south-central Pyrenees): an example of a flood-dominated river delta system in a tectonically controlled basin. *Riv. It. Paleo. Strat.*, **113**, 223–255.
- Tinterri, R.** (2011) Combined flow sedimentary structures and the genetic link between sigmoidal- and hummocky-cross stratification. *GeoActa*, **10**, 43–85.
- Tinterri, R. and Muzzi Magalhaes, P.** (2011) Synsedimentary structural control on foredeep turbidites related to basin segmentation: facies response to the increase in tectonic confinement (Marnoso-arenacea Formation, Miocene, Northern Apennines, Italy). *Mar. Petrol. Geol.*, **67**, 81–110.
- Tinterri, R., Muzzi Magalhaes, P., Tagliaferri, A. and Cunha, R.S.** (2016) Convolute laminations and load structures in turbidites as indicators of flow reflections and decelerations against bounding slopes. Examples from the Marnoso-arenacea Formation (northern Italy) and Annot Sandstones (south eastern France). *Sed. Geol.*, **344**, 382–407.
- Tinterri, R., Mazza, T. and Muzzi Magalhaes, P.** (2022) Contained-reflected megaturbidites of the Marnoso-arenacea Formation (Contessa Key Bed) and Helminthoid Flysches (Northern Apennines, Italy) and Hecho Group (South-Western Pyrenees). *Front. Earth Sci.*, **25**, 817012.
- Tomasso, M. and Sinclair, H.D.** (2004) Deep-water sedimentation of an evolving fault-block: the Braux and St Benoit outcrops of the Grès d'Annot. In: *Deep-Water Sedimentation in the Alpine Basin of SE France: New Perspectives on the Grès d'Annot and Related Systems* (Eds Joseph, P. and Lomas, S.A.), Vol. **221**, pp. 267–283. Geological Society, Bath, UK.
- Toniolo, H., Lamb, M. and Parker, G.** (2006) Depositional turbidity currents in diapiric minibasins on the continental slope: formation and theory. *J. Sed. Res.*, **76**, 783–797.
- Wu, X., Carling, P.A. and Parsons, D.** (2024) Hummocky sedimentary structures within rippled beds due to combined orbital waves and transverse currents. *Sedimentology*, **71**, 573–589.
- Yalin, M.S.** (1971) *Theory of Hydraulic Models*. Macmillan, London, UK. 266 pp.
- Yokokawa, M.** (1995) Combined flow ripples: genetic experiments and applications for geologic records. Kyushu University, Faculty of Science, Memoirs, Series D, Earth and Planetary Sciences, **29**, 1–38.

Manuscript received 31 January 2024; revision accepted 16 July 2024

Supporting Information

Additional information may be found in the online version of this article:

Table S1. Reynolds Number (Re) and Densimetric Froude Number (Fr_d) calculations. The Ultrasonic velocimeter Doppler profiler (UVP) measurements were recorded 3 m downstream of the channel mouth, along the flow's axis, and were initiated 5 s after the head of the unconfined passed, and lasted 30 s.